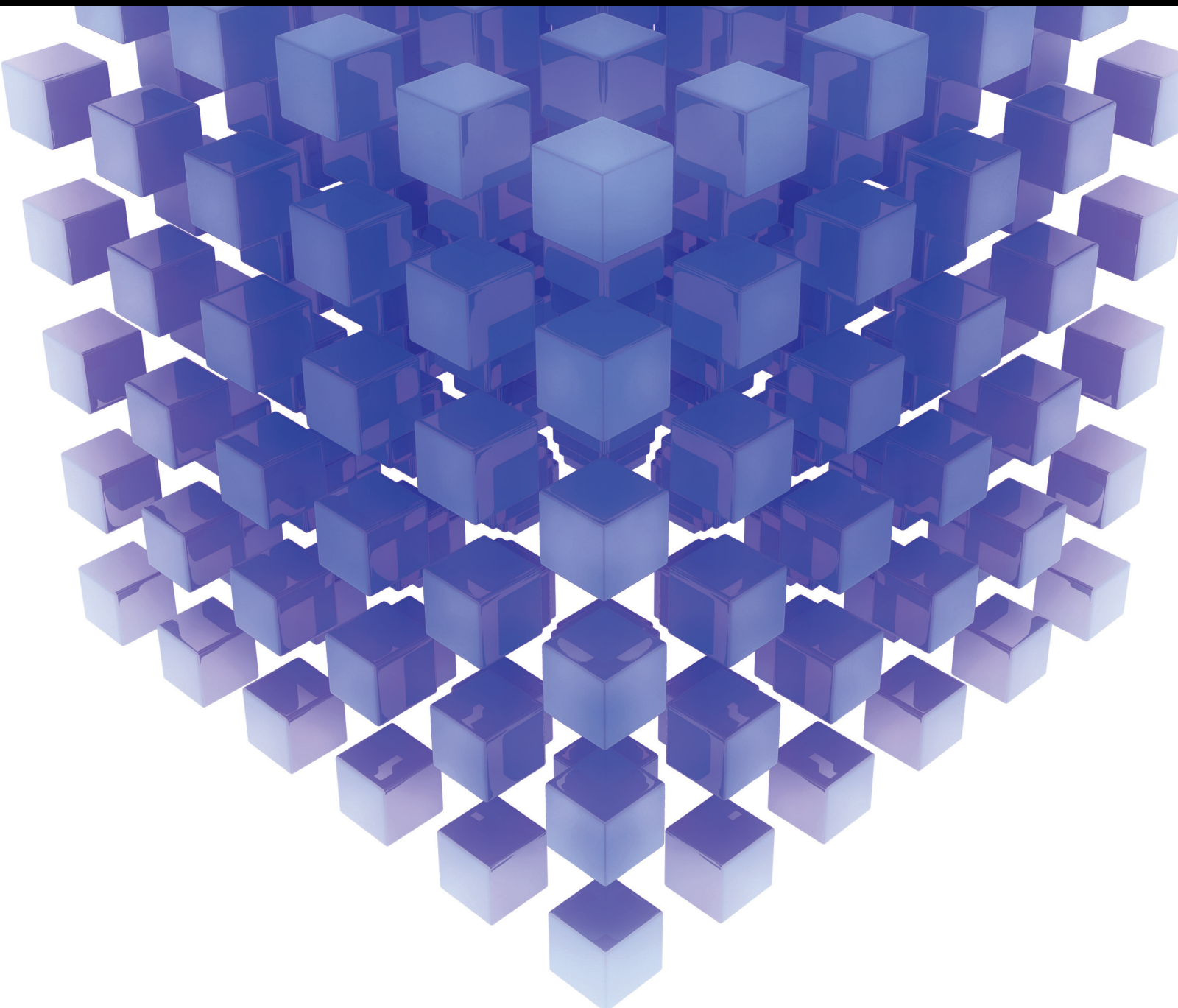


Mathematical Problems in Engineering

Advanced Computational Methods for Hydraulic Fracturing

Lead Guest Editor: Guowen Xu

Guest Editors: Jie Chen and Zhenkun Hou





Advanced Computational Methods for Hydraulic Fracturing

Mathematical Problems in Engineering

Advanced Computational Methods for Hydraulic Fracturing

Lead Guest Editor: Guowen Xu


Guest Editors: Jie Chen and Zhenkun Hou



Copyright © 2021 Hindawi Limited. All rights reserved.

This is a special issue published in “Mathematical Problems in Engineering.” All articles are open access articles distributed under the Creative Commons Attribution License, which permits unrestricted use, distribution, and reproduction in any medium, provided the original work is properly cited.

Chief Editor

Guangming Xie , China

Academic Editors

Kumaravel A , India
Waqas Abbasi, Pakistan
Mohamed Abd El Aziz , Egypt
Mahmoud Abdel-Aty , Egypt
Mohammed S. Abdo, Yemen
Mohammad Yaghoub Abdollahzadeh
Jamalabadi , Republic of Korea
Rahib Abiyev , Turkey
Leonardo Acho , Spain
Daniela Addessi , Italy
Arooj Adeel , Pakistan
Waleed Adel , Egypt
Ramesh Agarwal , USA
Francesco Aggogeri , Italy
Ricardo Aguilar-Lopez , Mexico
Afaq Ahmad , Pakistan
Naveed Ahmed , Pakistan
Elias Aifantis , USA
Akif Akgul , Turkey
Tareq Al-shami , Yemen
Guido Ala, Italy
Andrea Alaimo , Italy
Reza Alam, USA
Osamah Albahri , Malaysia
Nicholas Alexander , United Kingdom
Salvatore Alfonzetti, Italy
Ghous Ali , Pakistan
Nouman Ali , Pakistan
Mohammad D. Aliyu , Canada
Juan A. Almendral , Spain
A.K. Alomari, Jordan
José Domingo Álvarez , Spain
Cláudio Alves , Portugal
Juan P. Amezcua-Sanchez, Mexico
Mukherjee Amitava, India
Lionel Amodeo, France
Sebastian Anita, Romania
Costanza Arico , Italy
Sabri Arik, Turkey
Fausto Arpino , Italy
Rashad Asharabi , Saudi Arabia
Farhad Aslani , Australia
Mohsen Asle Zaem , USA

Andrea Avanzini , Italy
Richard I. Avery , USA
Viktor Avrutin , Germany
Mohammed A. Awadallah , Malaysia
Francesco Aymerich , Italy
Sajad Azizi , Belgium
Michele Bacciocchi , Italy
Seungik Baek , USA
Khaled Bahlali, France
M.V.A Raju Bahubalendruni, India
Pedro Balaguer , Spain
P. Balasubramaniam, India
Stefan Balint , Romania
Ines Tejado Balsera , Spain
Alfonso Banos , Spain
Jerzy Baranowski , Poland
Tudor Barbu , Romania
Andrzej Bartoszewicz , Poland
Sergio Baselga , Spain
S. Caglar Baslamisli , Turkey
David Bassir , France
Chiara Bedon , Italy
Azeddine Beghdadi, France
Andriette Bekker , South Africa
Francisco Beltran-Carbajal , Mexico
Abdellatif Ben Makhlof , Saudi Arabia
Denis Benasciutti , Italy
Ivano Benedetti , Italy
Rosa M. Benito , Spain
Elena Benvenuti , Italy
Giovanni Berselli, Italy
Michele Betti , Italy
Pietro Bia , Italy
Carlo Bianca , France
Simone Bianco , Italy
Vincenzo Bianco, Italy
Vittorio Bianco, Italy
David Bigaud , France
Sardar Muhammad Bilal , Pakistan
Antonio Bilotta , Italy
Sylvio R. Bistafa, Brazil
Chiara Boccaletti , Italy
Rodolfo Bontempo , Italy
Alberto Borboni , Italy
Marco Bortolini, Italy

Paolo Boscariol, Italy
Daniela Boso , Italy
Guillermo Botella-Juan, Spain
Abdesselem Boulkroune , Algeria
Boulaïd Boulkroune, Belgium
Fabio Bovenga , Italy
Francesco Braghin , Italy
Ricardo Branco, Portugal
Julien Bruchon , France
Matteo Bruggi , Italy
Michele Brun , Italy
Maria Elena Bruni, Italy
Maria Angela Butturi , Italy
Bartłomiej Błachowski , Poland
Dhanamjayulu C , India
Raquel Caballero-Águila , Spain
Filippo Cacace , Italy
Salvatore Caddemi , Italy
Zuowei Cai , China
Roberto Caldelli , Italy
Francesco Cannizzaro , Italy
Maosen Cao , China
Ana Carpio, Spain
Rodrigo Carvajal , Chile
Caterina Casavola, Italy
Sara Casciati, Italy
Federica Caselli , Italy
Carmen Castillo , Spain
Inmaculada T. Castro , Spain
Miguel Castro , Portugal
Giuseppe Catalanotti , United Kingdom
Alberto Cavallo , Italy
Gabriele Cazzulani , Italy
Fatih Vehbi Celebi, Turkey
Miguel Cerrolaza , Venezuela
Gregory Chagnon , France
Ching-Ter Chang , Taiwan
Kuei-Lun Chang , Taiwan
Qing Chang , USA
Xiaoheng Chang , China
Prasenjit Chatterjee , Lithuania
Kacem Chehdi, France
Peter N. Cheimets, USA
Chih-Chiang Chen , Taiwan
He Chen , China





















Kebing Chen , China
Mengxin Chen , China
Shyi-Ming Chen , Taiwan
Xizhong Chen , Ireland
Xue-Bo Chen , China
Zhiwen Chen , China
Qiang Cheng, USA
Zeyang Cheng, China
Luca Chiapponi , Italy
Francisco Chicano , Spain
Tirivanhu Chinyoka , South Africa
Adrian Chmielewski , Poland
Seongim Choi , USA
Gautam Choubey , India
Hung-Yuan Chung , Taiwan
Yusheng Ci, China
Simone Cinquemani , Italy
Roberto G. Citarella , Italy
Joaquim Ciurana , Spain
John D. Clayton , USA
Piero Colajanni , Italy
Giuseppina Colicchio, Italy
Vassilios Constantoudis , Greece
Enrico Conte, Italy
Alessandro Contento , USA
Mario Cools , Belgium
Gino Cortellessa, Italy
Carlo Cosentino , Italy
Paolo Crippa , Italy
Erik Cuevas , Mexico
Guozeng Cui , China
Mehmet Cunkas , Turkey
Giuseppe D'Aniello , Italy
Peter Dabnichki, Australia
Weizhong Dai , USA
Zhifeng Dai , China
Purushothaman Damodaran , USA
Sergey Dashkovskiy, Germany
Adiel T. De Almeida-Filho , Brazil
Fabio De Angelis , Italy
Samuele De Bartolo , Italy
Stefano De Miranda , Italy
Filippo De Monte , Italy

José António Fonseca De Oliveira
Correia , Portugal
Jose Renato De Sousa , Brazil
Michael Defoort, France
Alessandro Della Corte, Italy
Laurent Dewasme , Belgium
Sanku Dey , India
Gianpaolo Di Bona , Italy
Roberta Di Pace , Italy
Francesca Di Puccio , Italy
Ramón I. Diego , Spain
Yannis Dimakopoulos , Greece
Hasan Dinçer , Turkey
José M. Domínguez , Spain
Georgios Dounias, Greece
Bo Du , China
Emil Dumic, Croatia
Madalina Dumitriu , United Kingdom
Premraj Durairaj , India
Saeed Eftekhari Azam, USA
Said El Kafhali , Morocco
Antonio Elipse , Spain
R. Emre Erkmen, Canada
John Escobar , Colombia
Leandro F. F. Miguel , Brazil
FRANCESCO FOTI , Italy
Andrea L. Facci , Italy
Shahla Faisal , Pakistan
Giovanni Falsone , Italy
Hua Fan, China
Jianguang Fang, Australia
Nicholas Fantuzzi , Italy
Muhammad Shahid Farid , Pakistan
Hamed Faruqi, Iran
Yann Favennec, France
Fiorenzo A. Fazzolari , United Kingdom
Giuseppe Fedele , Italy
Roberto Fedele , Italy
Baowei Feng , China
Mohammad Ferdows , Bangladesh
Arturo J. Fernández , Spain
Jesus M. Fernandez Oro, Spain
Francesco Ferrise, Italy
Eric Feulvarch , France
Thierry Floquet, France















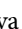








Eric Florentin , France
Gerardo Flores, Mexico
Antonio Forcina , Italy
Alessandro Formisano, Italy
Francesco Franco , Italy
Elisa Francomano , Italy
Juan Frausto-Solis, Mexico
Shujun Fu , China
Juan C. G. Prada , Spain
HECTOR GOMEZ , Chile
Matteo Gaeta , Italy
Mauro Gaggero , Italy
Zoran Gajic , USA
Jaime Gallardo-Alvarado , Mexico
Mosè Gallo , Italy
Akemi Gálvez , Spain
Maria L. Gandarias , Spain
Hao Gao , Hong Kong
Xingbao Gao , China
Yan Gao , China
Zhiwei Gao , United Kingdom
Giovanni Garcea , Italy
José García , Chile
Harish Garg , India
Alessandro Gasparetto , Italy
Stylianos Georgantzinou, Greece
Fotios Georgiades , India
Parviz Ghadimi , Iran
Ştefan Cristian Gherghina , Romania
Georgios I. Giannopoulos , Greece
Agathoklis Giaralis , United Kingdom
Anna M. Gil-Lafuente , Spain
Ivan Giorgio , Italy
Gaetano Giunta , Luxembourg
Jefferson L.M.A. Gomes , United Kingdom
Emilio Gómez-Déniz , Spain
Antonio M. Gonçalves de Lima , Brazil
Qunxi Gong , China
Chris Goodrich, USA
Rama S. R. Gorla, USA
Veena Goswami , India
Xunjie Gou , Spain
Jakub Grabski , Poland

Antoine Grall , France
George A. Gravvanis , Greece
Fabrizio Greco , Italy
David Greiner , Spain
Jason Gu , Canada
Federico Guarracino , Italy
Michele Guida , Italy
Muhammet Gul , Turkey
Dong-Sheng Guo , China
Hu Guo , China
Zhaoxia Guo, China
Yusuf Gurefe, Turkey
Salim HEDDAM , Algeria
ABID HUSSANAN, China
Quang Phuc Ha, Australia
Li Haitao , China
Petr Hájek , Czech Republic
Mohamed Hamdy , Egypt
Muhammad Hamid , United Kingdom
Renke Han , United Kingdom
Weimin Han , USA
Xingsi Han, China
Zhen-Lai Han , China
Thomas Hanne , Switzerland
Xinan Hao , China
Mohammad A. Hariri-Ardebili , USA
Khalid Hattaf , Morocco
Defeng He , China
Xiao-Qiao He, China
Yanchao He, China
Yu-Ling He , China
Ramdane Hedjar , Saudi Arabia
Jude Hemanth , India
Reza Hemmati, Iran
Nicolae Herisanu , Romania
Alfredo G. Hernández-Díaz , Spain
M.I. Herreros , Spain
Eckhard Hitzer , Japan
Paul Honeine , France
Jaromir Horacek , Czech Republic
Lei Hou , China
Yingkun Hou , China
Yu-Chen Hu , Taiwan
Yunfeng Hu, China
Can Huang , China
Gordon Huang , Canada
Linsheng Huo , China
Sajid Hussain, Canada
Asier Ibeas , Spain
Orest V. Iftime , The Netherlands
Przemyslaw Ignaciuk , Poland
Giacomo Innocenti , Italy
Emilio Insfran Pelozo , Spain
Azeem Irshad, Pakistan
Alessio Ishizaka, France
Benjamin Ivorra , Spain
Breno Jacob , Brazil
Reema Jain , India
Tushar Jain , India
Amin Jajarmi , Iran
Chiranjibe Jana , India
Łukasz Jankowski , Poland
Samuel N. Jator , USA
Juan Carlos Jáuregui-Correa , Mexico
Kandasamy Jayakrishna, India
Reza Jazar, Australia
Khalide Jbilou, France
Isabel S. Jesus , Portugal
Chao Ji , China
Qing-Chao Jiang , China
Peng-fei Jiao , China
Ricardo Fabricio Escobar Jiménez , Mexico
Emilio Jiménez Macías , Spain
Maolin Jin, Republic of Korea
Zhuo Jin, Australia
Ramash Kumar K , India
BHABEN KALITA , USA
MOHAMMAD REZA KHEDMATI , Iran
Viacheslav Kalashnikov , Mexico
Mathiyalagan Kalidass , India
Tamas Kalmar-Nagy , Hungary
Rajesh Kaluri , India
Jyotheeswara Reddy Kalvakurthi, India
Zhao Kang , China
Ramani Kannan , Malaysia
Tomasz Kapitaniak , Poland
Julius Kaplunov, United Kingdom
Konstantinos Karamanos, Belgium
Michal Kawulok, Poland

Irfan Kaymaz , Turkey
Vahid Kayvanfar , Qatar
Krzysztof Kecik , Poland
Mohamed Khader , Egypt
Chaudry M. Khalique , South Africa
Mukhtaj Khan , Pakistan
Shahid Khan , Pakistan
Nam-Il Kim, Republic of Korea
Philipp V. Kiryukhantsev-Korneev ,
Russia
P.V.V Kishore , India
Jan Koci , Czech Republic
Ioannis Kostavelis , Greece
Sotiris B. Kotsiantis , Greece
Frederic Kratz , France
Vamsi Krishna , India
Edyta Kucharska, Poland
Krzysztof S. Kulpa , Poland
Kamal Kumar, India
Prof. Ashwani Kumar , India
Michal Kunicki , Poland
Cedrick A. K. Kwuimy , USA
Kyandoghere Kyamakya, Austria
Ivan Kyrchei , Ukraine
Márcio J. Lacerda , Brazil
Eduardo Lalla , The Netherlands
Giovanni Lancioni , Italy
Jaroslaw Latalski , Poland
Hervé Laurent , France
Agostino Lauria , Italy
Aimé Lay-Ekuakille , Italy
Nicolas J. Leconte , France
Kun-Chou Lee , Taiwan
Dimitri Lefebvre , France
Eric Lefevre , France
Marek Lefik, Poland
Yaguo Lei , China
Kauko Leiviskä , Finland
Ervin Lenzi , Brazil
ChenFeng Li , China
Jian Li , USA
Jun Li , China
Yueyang Li , China
Zhao Li , China































Zhen Li , China
En-Qiang Lin, USA
Jian Lin , China
Qibin Lin, China
Yao-Jin Lin, China
Zhiyun Lin , China
Bin Liu , China
Bo Liu , China
Heng Liu , China
Jianxu Liu , Thailand
Lei Liu , China
Sixin Liu , China
Wanquan Liu , China
Yu Liu , China
Yuanchang Liu , United Kingdom
Bonifacio Llamazares , Spain
Alessandro Lo Schiavo , Italy
Jean Jacques Loiseau , France
Francesco Lolli , Italy
Paolo Lonetti , Italy
António M. Lopes , Portugal
Sebastian López, Spain
Luis M. López-Ochoa , Spain
Vassilios C. Loukopoulos, Greece
Gabriele Maria Lozito , Italy
Zhiguo Luo , China
Gabriel Luque , Spain
Valentin Lychagin, Norway
YUE MEI, China
Junwei Ma , China
Xuanlong Ma , China
Antonio Madeo , Italy
Alessandro Magnani , Belgium
Toqeer Mahmood , Pakistan
Fazal M. Mahomed , South Africa
Arunava Majumder , India
Sarfranz Nawaz Malik, Pakistan
Paolo Manfredi , Italy
Adnan Maqsood , Pakistan
Muazzam Maqsood, Pakistan
Giuseppe Carlo Marano , Italy
Damijan Markovic, France
Filipe J. Marques , Portugal
Luca Martinelli , Italy
Denizar Cruz Martins, Brazil

Francisco J. Martos , Spain
Elio Masciari , Italy
Paolo Massioni , France
Alessandro Mauro , Italy
Jonathan Mayo-Maldonado , Mexico
Pier Luigi Mazzeo , Italy
Laura Mazzola, Italy
Driss Mehdi , France
Zahid Mehmood , Pakistan
Roderick Melnik , Canada
Xiangyu Meng , USA
Jose Merodio , Spain
Alessio Merola , Italy
Mahmoud Mesbah , Iran
Luciano Mescia , Italy
Laurent Mevel , France
Constantine Michailides , Cyprus
Mariusz Michta , Poland
Prankul Middha, Norway
Aki Mikkola , Finland
Giovanni Minafò , Italy
Edmondo Minisci , United Kingdom
Hiroyuki Mino , Japan
Dimitrios Mitsotakis , New Zealand
Ardashir Mohammadzadeh , Iran
Francisco J. Montáns , Spain
Francesco Montefusco , Italy
Gisele Mophou , France
Rafael Morales , Spain
Marco Morandini , Italy
Javier Moreno-Valenzuela , Mexico
Simone Morganti , Italy
Caroline Mota , Brazil
Aziz Moukrim , France
Shen Mouquan , China
Dimitris Mourtzis , Greece
Emiliano Mucchi , Italy
Taseer Muhammad, Saudi Arabia
Ghulam Muhiuddin, Saudi Arabia
Amitava Mukherjee , India
Josefa Mula , Spain
Jose J. Muñoz , Spain
Giuseppe Muscolino, Italy
Marco Mussetta , Italy

Hariharan Muthusamy, India
Alessandro Naddeo , Italy
Raj Nandkeolyar, India
Keivan Navaie , United Kingdom
Soumya Nayak, India
Adrian Neagu , USA
Erivelton Geraldo Nepomuceno , Brazil
AMA Neves, Portugal
Ha Quang Thinh Ngo , Vietnam
Nhon Nguyen-Thanh, Singapore
Papakostas Nikolaos , Ireland
Jelena Nikolic , Serbia
Tatsushi Nishi, Japan
Shanzhou Niu , China
Ben T. Nohara , Japan
Mohammed Nouari , France
Mustapha Nourelfath, Canada
Kazem Nouri , Iran
Ciro Núñez-Gutiérrez , Mexico
Włodzimierz Ogryczak, Poland
Roger Ohayon, France
Krzysztof Okarma , Poland
Mitsuhiro Okayasu, Japan
Murat Olgun , Turkey
Diego Oliva, Mexico
Alberto Olivares , Spain
Enrique Onieva , Spain
Calogero Orlando , Italy
Susana Ortega-Cisneros , Mexico
Sergio Ortobelli, Italy
Naohisa Otsuka , Japan
Sid Ahmed Ould Ahmed Mahmoud , Saudi Arabia
Taoreed Owolabi , Nigeria
EUGENIA PETROPOULOU , Greece
Arturo Pagano, Italy
Madhumangal Pal, India
Pasquale Palumbo , Italy
Dragan Pamučar, Serbia
Weifeng Pan , China
Chandan Pandey, India
Rui Pang, United Kingdom
Jürgen Pannek , Germany
Elena Panteley, France
Achille Paolone, Italy

George A. Papakostas , Greece
Xosé M. Pardo , Spain
You-Jin Park, Taiwan
Manuel Pastor, Spain
Pubudu N. Pathirana , Australia
Surajit Kumar Paul , India
Luis Payá , Spain
Igor Pažanin , Croatia
Libor Pekař , Czech Republic
Francesco Pellicano , Italy
Marcello Pellicciari , Italy
Jian Peng , China
Mingshu Peng, China
Xiang Peng , China
Xindong Peng, China
Yuexing Peng, China
Marzio Pennisi , Italy
Maria Patrizia Pera , Italy
Matjaz Perc , Slovenia
A. M. Bastos Pereira , Portugal
Wesley Peres, Brazil
F. Javier Pérez-Pinal , Mexico
Michele Perrella, Italy
Francesco Pesavento , Italy
Francesco Petrini , Italy
Hoang Vu Phan, Republic of Korea
Lukasz Pieczonka , Poland
Dario Piga , Switzerland
Marco Pizzarelli , Italy
Javier Plaza , Spain
Goutam Pohit , India
Dragan Poljak , Croatia
Jorge Pomares , Spain
Hiram Ponce , Mexico
Sébastien Poncet , Canada
Volodymyr Ponomaryov , Mexico
Jean-Christophe Ponsart , France
Mauro Pontani , Italy
Sivakumar Poruran, India
Francesc Pozo , Spain
Aditya Rio Prabowo , Indonesia
Anchasa Pramuanjaroenkij , Thailand
Leonardo Primavera , Italy
B Rajanarayan Prusty, India

Krzysztof Puszynski , Poland
Chuan Qin , China
Dongdong Qin, China
Jianlong Qiu , China
Giuseppe Quaranta , Italy
DR. RITU RAJ , India
Vitomir Racic , Italy
Carlo Rainieri , Italy
Kumbakonam Ramamani Rajagopal, USA
Ali Ramazani , USA
Angel Manuel Ramos , Spain
Higinio Ramos , Spain
Muhammad Afzal Rana , Pakistan
Muhammad Rashid, Saudi Arabia
Manoj Rastogi, India
Alessandro Rasulo , Italy
S.S. Ravindran , USA
Abdolrahman Razani , Iran
Alessandro Reali , Italy
Jose A. Reinoso , Spain
Oscar Reinoso , Spain
Haijun Ren , China
Carlo Renno , Italy
Fabrizio Renno , Italy
Shahram Rezapour , Iran
Ricardo Rianza , Spain
Francesco Riganti-Fulginei , Italy
Gerasimos Rigatos , Greece
Francesco Ripamonti , Italy
Jorge Rivera , Mexico
Eugenio Roanes-Lozano , Spain
Ana Maria A. C. Rocha , Portugal
Luigi Rodino , Italy
Francisco Rodríguez , Spain
Rosana Rodríguez López, Spain
Francisco Rossomando , Argentina
Jose de Jesus Rubio , Mexico
Weiguo Rui , China
Rubén Ruiz , Spain
Ivan D. Rukhlenko , Australia
Dr. Eswaramoorthi S. , India
Weichao SHI , United Kingdom
Chaman Lal Sabharwal , USA
Andrés Sáez , Spain

Bekir Sahin, Turkey
Laxminarayan Sahoo , India
John S. Sakellariou , Greece
Michael Sakellariou , Greece
Salvatore Salamone, USA
Jose Vicente Salcedo , Spain
Alejandro Salcido , Mexico
Alejandro Salcido, Mexico
Nunzio Salerno , Italy
Rohit Salgotra , India
Miguel A. Salido , Spain
Sinan Salih , Iraq
Alessandro Salvini , Italy
Abdus Samad , India
Sovan Samanta, India
Nikolaos Samaras , Greece
Ramon Sancibrian , Spain
Giuseppe Sanfilippo , Italy
Omar-Jacobo Santos, Mexico
J Santos-Reyes , Mexico
José A. Sanz-Herrera , Spain
Musavarah Sarwar, Pakistan
Shahzad Sarwar, Saudi Arabia
Marcelo A. Savi , Brazil
Andrey V. Savkin, Australia
Tadeusz Sawik , Poland
Roberta Sburlati, Italy
Gustavo Scaglia , Argentina
Thomas Schuster , Germany
Hamid M. Sedighi , Iran
Mijanur Rahaman Seikh, India
Tapan Senapati , China
Lotfi Senhadji , France
Junwon Seo, USA
Michele Serpilli, Italy
Silvestar Šesnić , Croatia
Gerardo Severino, Italy
Ruben Sevilla , United Kingdom
Stefano Sfarra , Italy
Dr. Ismail Shah , Pakistan
Leonid Shaikhet , Israel
Vimal Shanmuganathan , India
Prayas Sharma, India
Bo Shen , Germany
Hang Shen, China

Xin Pu Shen, China
Dimitri O. Shepelsky, Ukraine
Jian Shi , China
Amin Shokrollahi, Australia
Suzanne M. Shontz , USA
Babak Shotorban , USA
Zhan Shu , Canada
Angelo Sifaleras , Greece
Nuno Simões , Portugal
Mehakpreet Singh , Ireland
Piyush Pratap Singh , India
Rajiv Singh, India
Seralathan Sivamani , India
S. Sivasankaran , Malaysia
Christos H. Skiadas, Greece
Konstantina Skouri , Greece
Neale R. Smith , Mexico
Bogdan Smolka, Poland
Delfim Soares Jr. , Brazil
Alba Sofi , Italy
Francesco Soldovieri , Italy
Raffaele Solimene , Italy
Yang Song , Norway
Jussi Sopanen , Finland
Marco Spadini , Italy
Paolo Spagnolo , Italy
Ruben Specogna , Italy
Vasilios Spitas , Greece
Ivanka Stamova , USA
Rafał Stanisławski , Poland
Miladin Stefanović , Serbia
Salvatore Strano , Italy
Yakov Strelniker, Israel
Kangkang Sun , China
Qiuqin Sun , China
Shuaishuai Sun, Australia
Yanchao Sun , China
Zong-Yao Sun , China
Kumarasamy Suresh , India
Sergey A. Suslov , Australia
D.L. Suthar, Ethiopia
D.L. Suthar , Ethiopia
Andrzej Swierniak, Poland
Andras Szekrenyes , Hungary
Kumar K. Tamma, USA

Yong (Aaron) Tan, United Kingdom
Marco Antonio Taneco-Hernández , Mexico
Lu Tang , China
Tianyou Tao, China
Hafez Tari , USA
Alessandro Tasora , Italy
Sergio Teggi , Italy
Adriana del Carmen Téllez-Anguiano , Mexico
Ana C. Teodoro , Portugal
Efstathios E. Theotokoglou , Greece
Jing-Feng Tian, China
Alexander Timokha , Norway
Stefania Tomasiello , Italy
Gisella Tomasini , Italy
Isabella Torricollo , Italy
Francesco Tornabene , Italy
Mariano Torrisi , Italy
Thang nguyen Trung, Vietnam
George Tsiatas , Greece
Le Anh Tuan , Vietnam
Nerio Tullini , Italy
Emilio Turco , Italy
Ilhan Tuzcu , USA
Efstratios Tzirtzilakis , Greece
FRANCISCO UREÑA , Spain
Filippo Ubertini , Italy
Mohammad Uddin , Australia
Mohammad Safi Ullah , Bangladesh
Serdar Ulubeyli , Turkey
Mati Ur Rahman , Pakistan
Panayiotis Vafeas , Greece
Giuseppe Vairo , Italy
Jesus Valdez-Resendiz , Mexico
Eusebio Valero, Spain
Stefano Valvano , Italy
Carlos-Renato Vázquez , Mexico
Martin Velasco Villa , Mexico
Franck J. Vernerey, USA
Georgios Veronis , USA
Vincenzo Vespri , Italy
Renato Vidoni , Italy
Venkatesh Vijayaraghavan, Australia

Anna Vila, Spain
Francisco R. Villatoro , Spain
Francesca Vipiana , Italy
Stanislav Vitek , Czech Republic
Jan Vorel , Czech Republic
Michael Vynnycky , Sweden
Mohammad W. Alomari, Jordan
Roman Wan-Wendner , Austria
Bingchang Wang, China
C. H. Wang , Taiwan
Dagang Wang, China
Guoqiang Wang , China
Huaiyu Wang, China
Hui Wang , China
J.G. Wang, China
Ji Wang , China
Kang-Jia Wang , China
Lei Wang , China
Qiang Wang, China
Qingling Wang , China
Weiwei Wang , China
Xinyu Wang , China
Yong Wang , China
Yung-Chung Wang , Taiwan
Zhenbo Wang , USA
Zhibo Wang, China
Waldemar T. Wójcik, Poland
Chi Wu , Australia
Qihong Wu, China
Yuqiang Wu, China
Zhibin Wu , China
Zhizheng Wu , China
Michalis Xenos , Greece
Hao Xiao , China
Xiao Ping Xie , China
Qingzheng Xu , China
Binghan Xue , China
Yi Xue , China
Joseph J. Yame , France
Chuanliang Yan , China
Xinggang Yan , United Kingdom
Hongtai Yang , China
Jixiang Yang , China
Mijia Yang, USA
Ray-Yeng Yang, Taiwan

Zaoli Yang , China
Jun Ye , China
Min Ye , China
Luis J. Yebra , Spain
Peng-Yeng Yin , Taiwan
Muhammad Haroon Yousaf , Pakistan
Yuan Yuan, United Kingdom
Qin Yuming, China
Elena Zaitseva , Slovakia
Arkadiusz Zak , Poland
Mohammad Zakwan , India
Ernesto Zambrano-Serrano , Mexico
Francesco Zammori , Italy
Jessica Zangari , Italy
Rafal Zdunek , Poland
Ibrahim Zeid, USA
Nianyin Zeng , China
Junyong Zhai , China
Hao Zhang , China
Haopeng Zhang , USA
Jian Zhang , China
Kai Zhang, China
Lingfan Zhang , China
Mingjie Zhang , Norway
Qian Zhang , China
Tianwei Zhang , China
Tongqian Zhang , China
Wenyu Zhang , China
Xianming Zhang , Australia
Xuping Zhang , Denmark
Yinyan Zhang, China
Yifan Zhao , United Kingdom
Debao Zhou, USA
Heng Zhou , China
Jian G. Zhou , United Kingdom
Junyong Zhou , China
Xueqian Zhou , United Kingdom
Zhe Zhou , China
Wu-Le Zhu, China
Gaetano Zizzo , Italy
Mingcheng Zuo, China



Contents

An Evaluation Method of Rock Brittleness Based on the Prepeak Crack Initiation and Postpeak Stress Drop Characteristics

Meiben Gao , Tianbin Li , and Lubo Meng 

Research Article (9 pages), Article ID 5639649, Volume 2021 (2021)

Numerical Investigation into the Distributions of Temperature and Stress around Wellbore during the Injection of Cryogenic Liquid Nitrogen into Hot Dry Rock Reservoir

Keda Ren  and Chengzheng Cai 

Research Article (13 pages), Article ID 9913321, Volume 2021 (2021)

Research Article

An Evaluation Method of Rock Brittleness Based on the Prepeak Crack Initiation and Postpeak Stress Drop Characteristics

Meiben Gao ^{1,2,3}, Tianbin Li ^{2,3} and Lubo Meng ^{2,3}

¹School of Emergency Science, Xihua University, Chengdu, Sichuan 610039, China

²State Key Laboratory of Geohazard Prevention and Geoenvironment Protection, Chengdu University of Technology, Chengdu, Sichuan 610059, China

³College of Environmental and Civil Engineering, Chengdu University of Technology, Chengdu, Sichuan 610059, China

Correspondence should be addressed to Tianbin Li; lbt@cdut.edu.cn

Received 22 May 2021; Accepted 16 July 2021; Published 23 July 2021

Academic Editor: Zhenkun Hou

Copyright © 2021 Meiben Gao et al. This is an open access article distributed under the Creative Commons Attribution License, which permits unrestricted use, distribution, and reproduction in any medium, provided the original work is properly cited.

Recent research shows that the brittleness of rock is closely related to the initiation and propagation of internal microcracks, but there are few brittleness evaluation indices considering the characteristics of rock initiation. Based on the theoretical analysis of brittleness and the characteristics of rock initiation, this study proposes an evaluation method of rock brittleness based on the prepeak crack initiation and postpeak stress drop characteristics. First, based on the description and definition of brittleness by George Tarasov and Potvin et al., the feasibility of an evaluation method based on the prepeak crack initiation and postpeak stress drop is theoretically analyzed. Second, the component B_i representing the prepeak brittleness of rock and component B_{ii} representing the postpeak brittleness of rock are constructed, and the product of the two is the brittleness index B_1 , representing the prepeak crack initiation and postpeak stress drop. Finally, experimental tests of granite and marble were conducted to evaluate the new index, and the brittleness indices of different methods are calculated and compared. The results show that, like other brittleness indices ($B_1 \sim B_5$), the brittleness index B_1 can effectively reflect the effects of different confining pressures and loading modes on rock brittleness. The brittleness of marble decreases with increasing confining pressure from 5 MPa to 35 MPa. At a confining pressure of 5 MPa, the brittleness of granite during a triaxial unloading test is greater than that during a triaxial compression test. The calculated results are consistent with the experimental results. By tests and comparison results, the reliability of this evaluation method was verified, which provides a way to evaluate rock brittleness from the perspective of crack initiation and is helpful to enrich the analysis and evaluation of rock brittleness in the laboratory.

1. Introduction

Rock brittleness, as one of the basic properties of rock, is a key index to evaluate rock properties. Accurate evaluation of rock brittleness is of great significance for guiding the effective development and utilization of coal, oil, and gas resources, underground engineering, construction, and geological disaster prevention and mitigation [1–11]. Brittleness is the comprehensive performance of rock under different stress and different environments. Although an internationally accepted definition of brittleness has not yet been established [12], various researchers have defined rock brittleness to suit different purposes. From the perspective of strain, Morley and Hetenyi defined brittleness as the loss of

material plasticity. From the perspective of strength [13, 14], Ramsay argued that brittle failure occurred when the cohesion of rock was destroyed [15]. Obert and Duvall suggested that brittleness is a feature describing the failure behavior of rock materials when the yield strength of the rock is reached or exceeded [16]. From the perspective of energy, Tarasov and Potvin argued that rock brittleness is the ability to self-maintain macroscopic damage through the energy balance in the postpeak stage [17]. In addition, Li et al. believed that brittleness was a comprehensive property of rock materials: the ability to generate local damage and develop spatial fractures under an internal nonuniform stress distribution caused by the inherent heterogeneity of the rock [18].

Over the past 50 years, according to brittleness characteristics, many quantitative evaluation methods for rock brittleness have been proposed, and the influencing factors have been analyzed. These brittleness indices generally fall into three categories: brittleness index based on physical tests [4, 19, 20], brittleness index based on rock mechanical tests [3, 17, 21–23], and brittleness indices based on other methods [24, 25]. For example, Rickman et al. suggested that brittleness increases with the increase in quartz minerals, based on which they proposed a brittleness index to quantify rock brittleness as a function of the amounts of quartz, carbonate, and clay minerals in rocks [26]. However, this method fails to evaluate the same rock under different stress states [22]. Porosity also affects rock brittleness. Jin et al. claimed that there is a global correlation between mineralogy-derived brittle indices and neutron porosity [20]. Based on rock compression and splitting tests, various brittleness indices were built considering stress, strain, and energy, such as the ratio of the compressive strength to tensile strength [21], the ratio of the difference between the peak strength and residual strength to the peak strength, and the ratio of peak strength to the crack initiation stress [9]. Meanwhile, Coates determined the brittleness by the ratio of the recoverable strain to the total strain [27]. Hajiabdolmajid and Kaiser introduced a plastic strain-dependent brittleness index that considers cohesion weakening and frictional strengthening [28]. Tarasov and Potvin proposed a brittleness index based on the complete stress-strain curve of the energy balance [17]. However, for brittleness indices based on stress, many scholars criticized that those indices have yielded contradictory results to those calculated from the perspective of strain or energy; furthermore, the results are not monotonic and continuous. In addition to the above limitations, rock brittleness can be affected by the stress state, and rocks may be less brittle and more ductile under high confining pressure conditions, so those indices are not suitable for complex stress environments [22]. Indices based on strain do not consider the postpeak characteristic, which is critical to characterize the brittle features [28, 29]. Other indices were derived based on penetration testing [24], point load testing [25], and Mohr's circle analysis [30]. These approaches also have some limitations, such as the specific equipment required for the sampling and testing of rock via penetration testing, leading to its limited use. There is a lack of sufficient evidence that the point load testing method is reasonable for determining the values of K_b for various rocks.

In recent years, with the further study of rock fractures, it has been found that the failure symptoms and fracture energy of brittle rock materials are closely related to internal crack initiation fractures [9, 21]. For example, George pointed out that rock brittleness refers to the ability of microcracks in rock to produce and cause nonpermanent deformation and continuous deformation [31]. The rock brittleness is related to microcracks, including the characteristics of stress and strain when the crack initiates. In addition, Tarasov and Potvin considered brittleness under compression as the ability of the rock to self-sustain macroscopic failure in the postpeak region due to the elastic

energy accumulated within the loaded material [17]. From this definition, it can be seen that the brittleness of rock is related to the accumulation of elastic energy. The whole process of rock failure can be regarded as the occurrence of the following processes: microcrack compaction, initiation, development, convergence and penetration, and energy accumulation and consumption. Before microcracks initiate or before the stress level is lower than the initiation stress level, the microcracks in the rock do not propagate, which correspond to the process of elastic accumulation. When the stress level is higher than the crack initiation, stress microcracks in the rock initiate and develop. After crack initiation, the work performed by the external load will be transformed into compression elastic energy and consumed energy to maintain crack propagation. The elastic energy of the rock will continue to increase, but the growth rate of the crack will decrease. When the stress level reaches the yield strength, the internal cracks of the rock propagate rapidly, and the work performed by the external load is mainly transformed into consumable energy. When the rock fails, the total energy of the external work performed is consumed by rock failure, and there is no excess elastic energy. It can be considered that before the microcrack initiates, the microcrack is closed and the external work is purely transformed into elastic energy; after that, the microcracks initiate and expand, and part of the loading work is converted into consumed energy until the final failure when the loading work is completely converted into consumed energy. Combining the definition of brittleness, following [17, 31], the microcrack development, and the energy conversion process during rock failure, it is considered that the rock brittleness can be evaluated from prepeak crack initiation and postpeak stress drop characteristics. For example, some scholars have established new indices from the perspective of crack initiation stress [9, 21]. However, it is rarely reported that an evaluation index of rock brittleness is established from the viewpoint of crack initiation strain. In this study, the evaluation of the prepeak brittleness of rock is established from the viewpoint of crack initiation strain, and then, the evaluation component of postpeak brittleness is established according to the postpeak stress drop characteristics. Then, the rock brittleness evaluation index based on prepeak crack initiation and postpeak stress drop characteristics are established by synthesizing the prepeak and postpeak brittleness evaluation components.

2. Methods

2.1. Analysis Method for the Characteristics of Prepeak Crack Initiation in Rock. At present, the main analysis methods of rock crack initiation characteristics are the observation method, crack volumetric strain method, and acoustic emission method. Among them, the crack volumetric strain method is the most widely used. In this study, the crack initiation characteristics of rock will be determined by the crack volumetric strain method.

The crack volumetric strain method was first proposed by Martin in his doctoral thesis [32]. The key to determining the crack initiation stress by this method is that the crack

volumetric strain (ε_{Vcrack}) is subtracted from the volumetric strain (ε_V) by the elastic volumetric strain ($\varepsilon_{Velastic}$). Among them, the volumetric strain (ε_V) is calculated by the axial (ε_{axial}) and lateral strain ($\varepsilon_{lateral}$) measured in the test. The elastic volumetric strain is calculated by the stress state (σ_1, σ_3) and elastic parameters (E, μ) in the corresponding stage of the test, and the formulas for calculating each strain are as follows:

$$\begin{aligned}\varepsilon_V &= \varepsilon_{axial} + 2\varepsilon_{lateral}, \\ \varepsilon_{Velastic} &= \frac{(1 - 2\mu)(\sigma_1 + \sigma_3)}{E}, \\ \varepsilon_{Vcrack} &= \varepsilon_V - \varepsilon_{Velastic}.\end{aligned}\quad (1)$$

Figure 1 shows the volumetric strain characteristics of a crack. Under pressure, the internal microcracks and voids in the rock are continuously compressed. At the stage of linear elastic deformation, the crack volume is compressed to the limit state, and the rock is similar to an isotropic material, with only elastic volumetric strain and no crack volumetric strain. After that, with the increase in stress, when the loading stress reaches the crack initiation stress, the internal crack begins to initiate and propagate, and the crack volume increases gradually.

2.2. Proposed Method Based on Prepeak Crack Initiation and Postpeak Stress Drop Characteristics. A reasonable brittleness index should fully consider the entire scope of rock behavior and as many of the effects of the mechanical parameters of the rock and external loading conditions as possible [6, 33]. For example, Xia et al. proposed a new brittleness definition based on the postpeak stress drop rate and the ratio of prepeak released elastic energy to total energy [33]. In this study, we propose a brittleness index considering prepeak crack initiation and postpeak stress drop characteristics.

2.2.1. Theoretical Analysis. In the process of rock compression, the crack initiation stress is the boundary point of crack compression and propagation. If rock brittleness represents the ability of the rock to maintain the accumulation of elastic energy in the crack compaction state [32], the elastic energy growth rate reaches the peak when the crack initiates; then, the microcrack propagates, and the growth rate decreases. If the crack initiation strain ε_{ci} (the strain corresponding to the crack initiation stress) is used to characterize the ability of a rock to be compacted and the difference ($\Delta \varepsilon = \varepsilon_c - \varepsilon_{ci}$) between the peak strain ε_c (the strain corresponding to peak stress) and the crack initiation strain ε_{ci} represents the ability of a crack in the rock to propagate, then the strain ratio ($\varepsilon_{ci}/\Delta \varepsilon$) can be used to characterize the ability of the rock to maintain the compaction state. The larger the initiation strain ε_{ci} is, the more compression work consumed by the rock, the greater the elastic energy accumulation, and the stronger the compaction of the cracks. The smaller $\Delta \varepsilon$ is, the faster the crack growth. The larger the

$\varepsilon_{ci}/\Delta \varepsilon$ is, the greater the ability of the rock to maintain the crack compaction state. Then, the prepeak brittleness characteristics of rocks can be characterized by $\varepsilon_{ci}/\Delta \varepsilon$ (Figure 2).

In general, there are two failure forms (I and II, as shown in Figure 3(a)) for rocks due to compression testing [34]. Type II failure is commonly considered unstable and brittle, and brittle hard rock often follows this deformation and failure model. Therefore, combined with the postpeak characteristics of the stress-strain curve, the greater the brittleness of the rock is, the greater the stress drop after the peak. As shown in Figure 3(b), the steeper the drop in the postpeak curve, the larger the area S is. The postpeak brittleness characteristics of the rock can be characterized by S/S_Δ (S_Δ is the red triangle area in Figure 3(b)). Points M and N represent the peak point and the beginning point of residual stress.

2.2.2. Brittleness Evaluation Method. The brittleness evaluation method based on prepeak crack initiation and postpeak stress drop characteristics is as follows:

- (a) According to the characteristics reflected by the stress-strain curve of rock, the brittleness characteristics of the rock can be judged qualitatively
- (b) Considering the experimental data, it can be used to identify the crack initiation strain ε_{ci}
- (c) Considering the peak strain ε_c , the prepeak brittleness component $\mathbf{B}_i = \varepsilon_{ci}/\Delta \varepsilon$ can be calculated
- (d) Considering the postpeak characteristics, the areas of S and S_Δ can be calculated, and then, the postpeak brittleness component $\mathbf{B}_{ii} = S/S_\Delta$ can be calculated; the value of \mathbf{B}_{ii} is between 0 and 1.
- (e) The brittleness index based on prepeak crack initiation and postpeak stress drop characteristics can be calculated as follows:

$$\mathbf{B}_I = \mathbf{B}_i \cdot \mathbf{B}_{ii}. \quad (2)$$

\mathbf{B}_i and \mathbf{B}_{ii} characterize the prepeak and postpeak brittleness characteristics of rock, respectively. There may be many combination modes that can be used to characterize the brittleness characteristics of rock by using these two components, such as in a sum form ($\mathbf{B}_a + \mathbf{B}_b$), a product form ($\mathbf{B}_a \cdot \mathbf{B}_b$), or other forms. Some scholars, such as [18, 21], take the sum of the two components as the brittleness index. Some scholars, such as [22, 35], take the product of the two components as the brittleness index. In this study, the brittleness evaluation index in the form of a product is mainly considered based on the following factors. As the prepeak brittleness evaluation component of $\mathbf{B}_i = \varepsilon_{ci}/\Delta \varepsilon$ is based on its ability to maintain the crack in the compacted state, generally, after yielding, the stress of brittle rock falls rapidly under a small strain, resulting in $\Delta \varepsilon$ being smaller than the early crack initiation strain ε_{ci} ; thus, the ratio \mathbf{B}_i is usually greater than 1. The postpeak brittleness evaluation component of \mathbf{B}_{ii} is less than 1. If taking the sum of the two

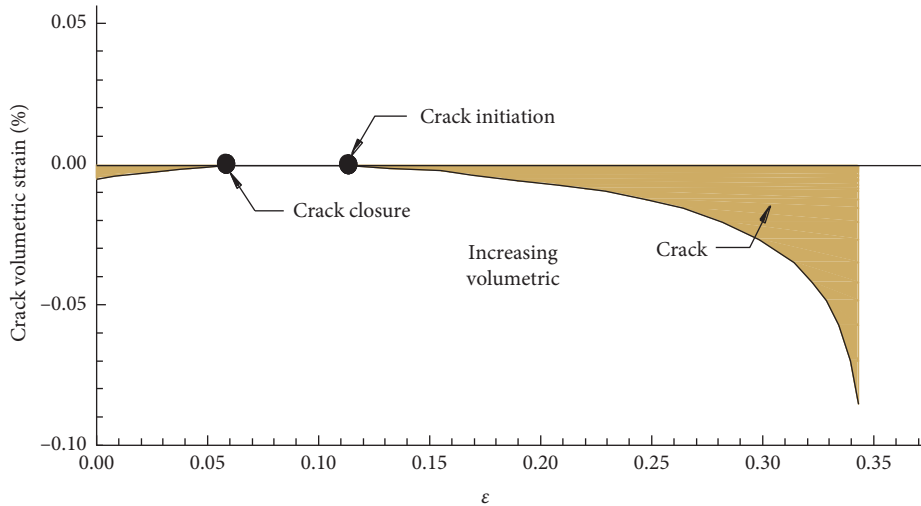


FIGURE 1: Crack volumetric strain characteristics.

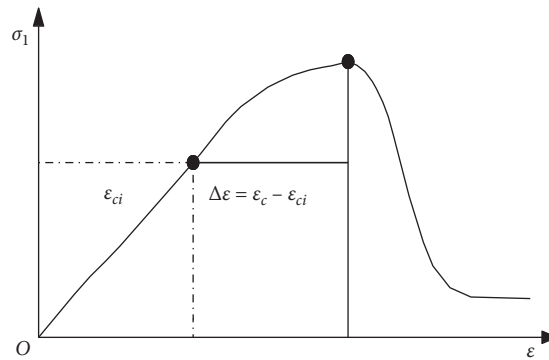


FIGURE 2: Schematic diagram of prepeak rock brittleness.

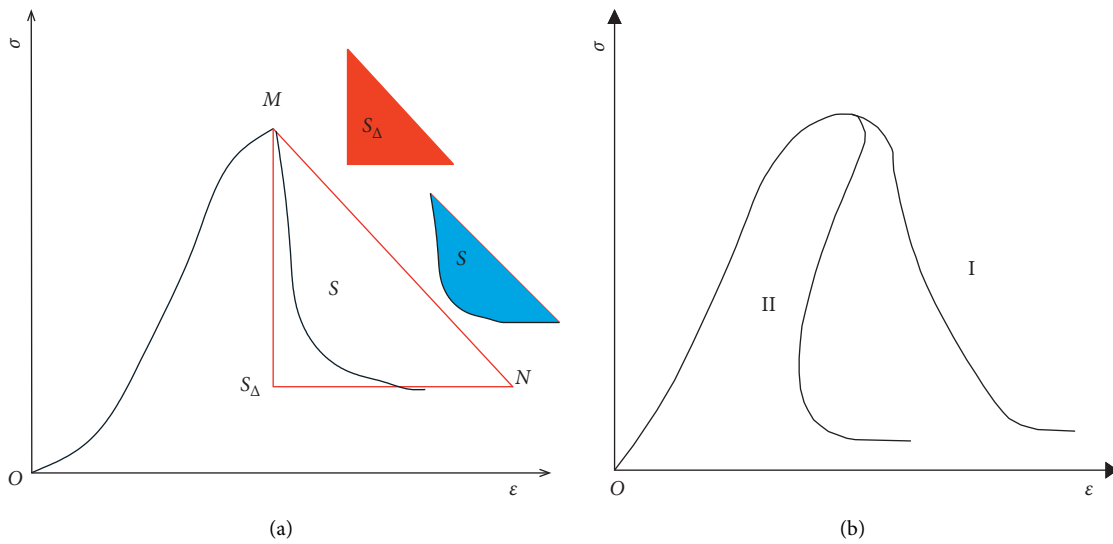


FIGURE 3: Schematic diagram of postpeak rock brittleness. (a) Rock failure mode [34]. (b) Postpeak brittleness characteristics.

$(\mathbf{B}_i + \mathbf{B}_{ii})$ as the brittleness evaluation index, it mainly reflects the prepeak brittleness characteristic because the value of the prepeak brittleness component \mathbf{B}_i may be much larger than

that of the postpeak brittle component \mathbf{B}_{ii} , which is unreasonable. If taking the product of the two $(\mathbf{B}_i \cdot \mathbf{B}_{ii})$ as the brittleness evaluation index, according to the theoretical

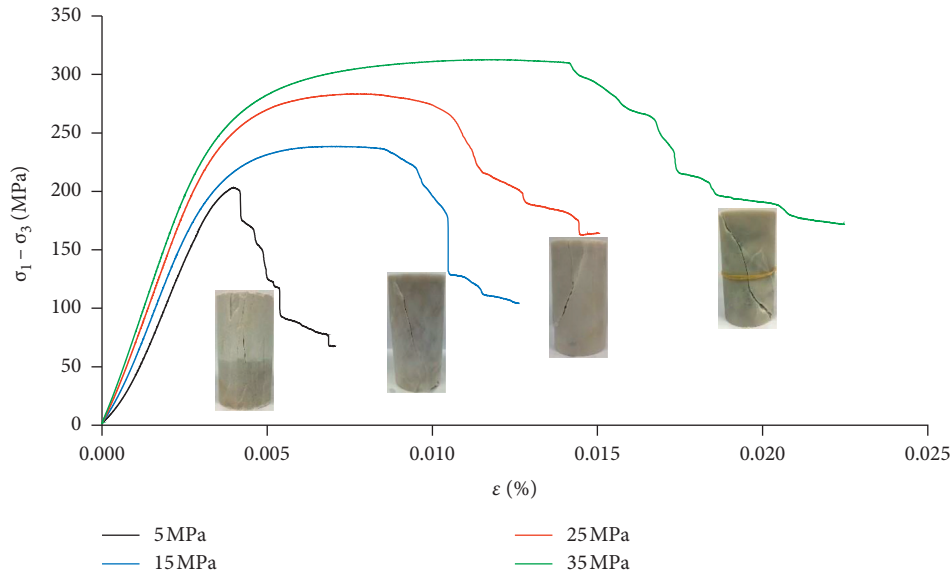


FIGURE 4: Marble test curves under different confining pressures.

analysis, the greater the brittleness of the rock is, the greater the B_i and B_{ii} values, and the greater the product of the two, which can eliminate the adverse effects of the obvious difference between the two components (B_i and B_{ii}). For example, if $B_i = 3$ and $B_{ii} = 0.1$ or 1 , their sum is 3.1 or 4 , but their product is 0.3 or 3 . From the example, we can see that taking the product of the two components as the brittleness evaluation index has the advantage of clearly categorizing the brittleness.

3. Verification of the Proposed Method

3.1. Verification of B_I under Different Confining Pressures. The triaxial compression test data of marble under different confining pressures were selected to verify the feasibility of this method. The test was carried out at Rock Mechanics Laboratory, State Key Laboratory of Geohazard Prevention and Geoenvironment Protection, Chengdu University of Technology. According to Figure 4, with increasing confining pressure, the plasticity of marble increases. At 5 MPa, the stress drops after the peak: first quickly and then more slowly, showing brittle failure. From 15 MPa to 35 MPa, with increasing confining pressure, the plastic deformation interval increases, and the plasticity increases. From a qualitative perspective, with increasing confining pressure, the plasticity of marble increases, which is consistent with previous research results [21, 22, 33, 35]. The calculation results of the brittleness index B_I under the corresponding conditions are given in Table 1. The values of the brittleness index B_I are 0.152, 0.110, 0.082, and 0.078 under 5~35 MPa. The calculated results are in good agreement with the experimental curve, which effectively reflects the variation in the brittleness index with confining pressure.

3.2. Verification of B_I under Different Loading Modes. In general, it is considered that rock brittleness is more obvious under unloading conditions than that under

conventional compressive loading conditions. Therefore, comparison analyses were conducted on the granite samples from the triaxial unloading test (5 MPa) and compressive test (5 MPa). According to Figure 5, for the unloading test under 5 MPa, the stress of the blue curve drops considerably after the peak point, indicating that the brittleness characteristic is prominent. For the compression test under 5 MPa, the stress of the green curve drops gradually after the peak point, showing strain-softening characteristics. The test results show that the brittleness of these granite samples under unloading conditions is larger than that under compressive loading conditions. The calculation results of the brittleness index B_I under different loading modes are given in Table 2. The B_I values are 0.94 and 0.40 for the unloading and compression tests, respectively. The calculated results are in good agreement with the experimental results. These results also effectively reflect the fact that the brittleness of rock under unloading conditions is stronger than that under loading conditions.

4. Discussion

At present, there are various rock brittleness indices. In this section, a comparison was made between the proposed brittleness index (B_I) and 5 commonly used brittleness indices. Because of the heterogeneity and anisotropy of rock materials, it is advisable to select the brittleness indices established based on the same sample or stress-strain curve as the object for comparative discussion and analysis. The formulas of the selected brittleness indices are given in Table 3. Figure 6 shows schematic diagrams for brittleness indices B_1 , B_2 , and B_5 .

In addition, a classification of rock brittleness has been established based on the research of brittleness index B_1 . There are 6 grades for rock brittleness, as given in Table 4.

TABLE 1: Calculation results of the brittleness index for marble under different confining pressures.

Confining pressure (MPa)	Peak strain $\varepsilon_c/\%$	Crack initiation strain $\varepsilon_{ci}/\%$	Strain difference $\Delta\varepsilon = \varepsilon_c - \varepsilon_{ci}$	B_i $\varepsilon_{ci}/\Delta\varepsilon$	B_{ii} S/S_Δ	B_I $B_I \cdot B_{ii}$	Qualitative analysis of the test curve
5	0.003980	0.001250	0.00273	0.46	0.33	0.152	Brittleness
15	0.007170	0.002170	0.00500	0.43	0.25	0.110	Elasticity-plasticity
25	0.007570	0.002440	0.00513	0.48	0.17	0.082	Elasticity-plasticity
35	0.011820	0.002730	0.00909	0.30	0.26	0.078	Elasticity-plasticity

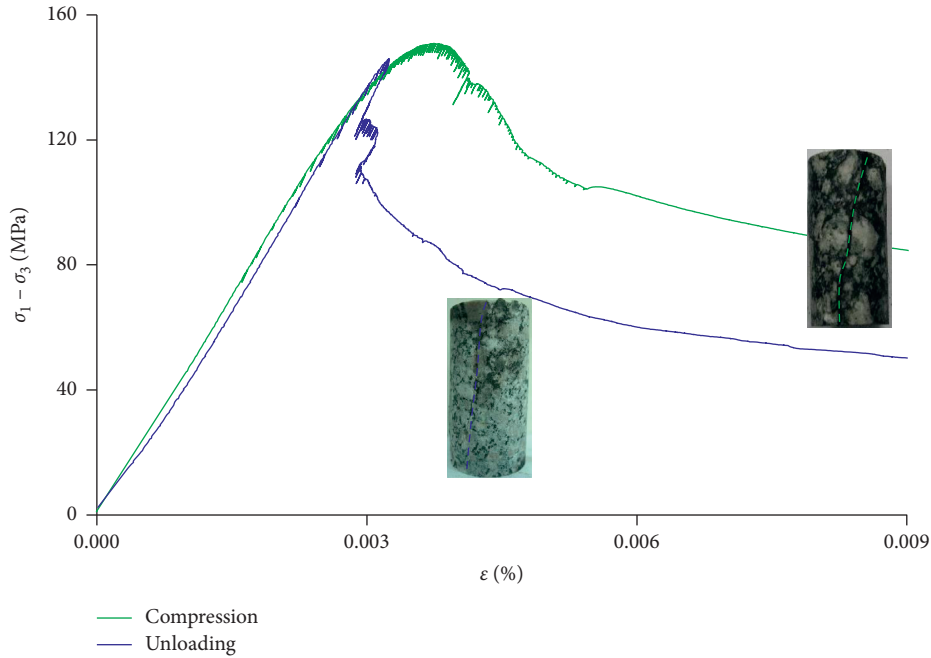


FIGURE 5: Granite test curves under different loading modes.

TABLE 2: Calculation results of the brittleness index of granite under different loading modes.

Loading modes	Peak strain $\varepsilon_c/\%$	Crack initiation strain $\varepsilon_{ci}/\%$	Strain difference $\Delta\varepsilon = \varepsilon_c - \varepsilon_{ci}$	B_i $\varepsilon_{ci}/\Delta\varepsilon$	B_{ii} S/S_Δ	B_I $B_I \cdot B_{ii}$	Qualitative analysis of the test curve
Unloading	0.003249	0.001828	0.001421	1.29	0.73	0.94	Brittleness
Compression	0.003746	0.001810	0.001936	0.93	0.43	0.40	Strain softening

TABLE 3: Brittleness indices for comparative analysis.

Brittleness	Calculation formula	Parameter specification
B_1	$B_1 = 1 - \exp(M/E)$ [36]	E is the prepeak elasticity modulus; M is the postpeak elasticity modulus
B_2	$B_2 = (\tau_p - \tau_r/\tau_p)(\lg k_{ac(AC)} /10)$ [35]	τ_p is the peak compressive strength; τ_r is the residual compressive strength; $k_{ac(AC)}$ is the slope of ac (AC).
B_3	$B_3 = (\tau_p - \tau_r)/\tau_p$ [12]	τ_p is the peak compressive strength; τ_r is the residual compressive strength.
B_4	$B_4 = (\varepsilon_p - \varepsilon_r)/\varepsilon_p$ [12]	ε_p is peak strain; ε_r is the residual strain
B_5	$B_5 = (\varepsilon_B - \varepsilon_P)/(\varepsilon_P - \varepsilon_M)$ [37]	ε_p is peak strain; ε_B is the residual strain; ε_M is the prepeak strain when the stress reaches the residual stress.

The brittleness evaluation results of B_I and $B_1 \sim B_5$ are compared and analyzed for different confining pressure loading modes.

The results for marble from the different brittleness evaluation methods are given in Table 5 for each confining pressure. According to Table 5, B_I and B_1 decrease with

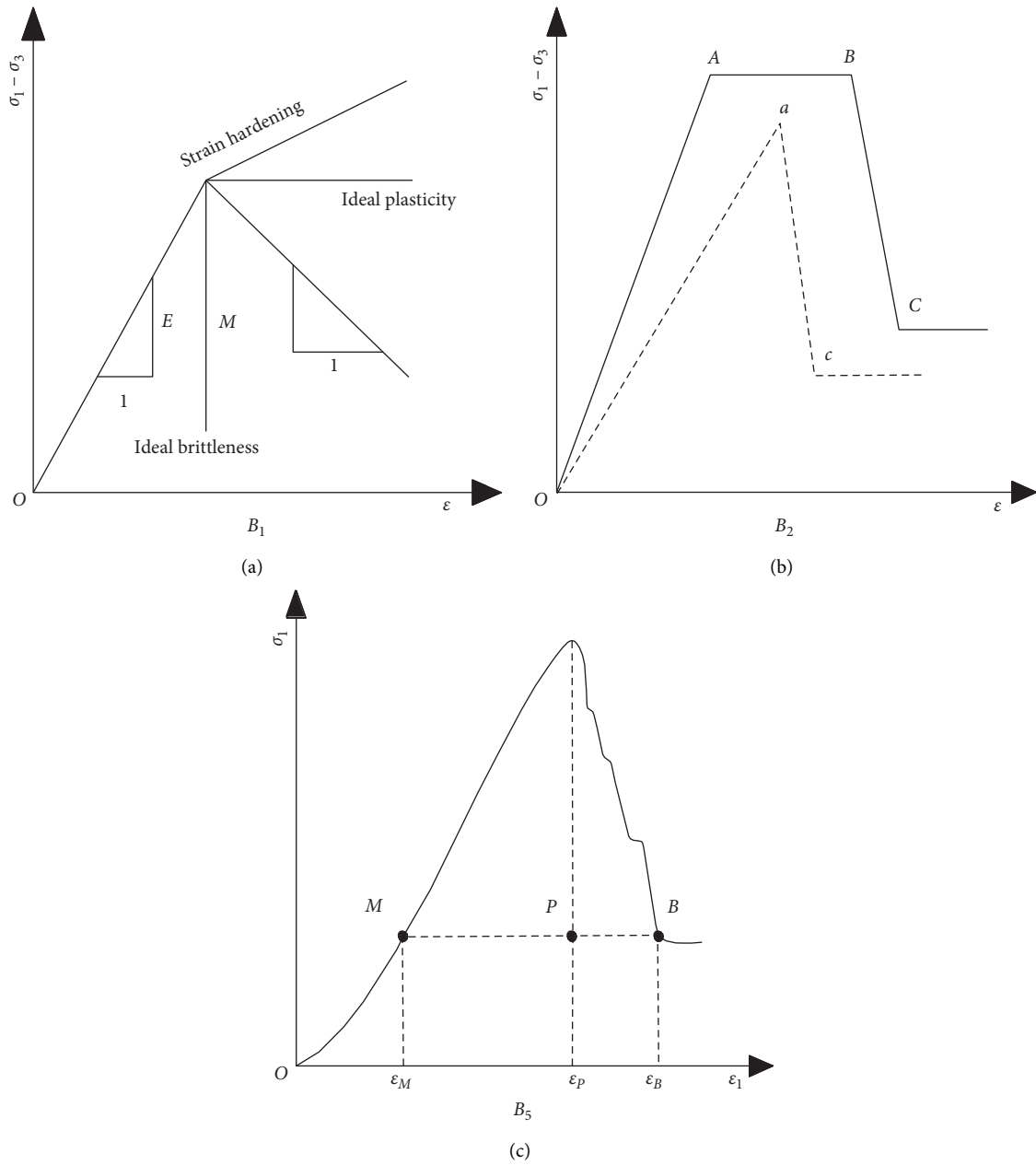


FIGURE 6: Schematic diagram of the calculation model of the partial brittleness evaluation index.

TABLE 4: Classification and description of brittleness index B_1 .

Grade	B_1	Description
1	1	$M \rightarrow -\infty$, ideal brittleness
2	0.6321~1	$-\infty < M < -E$, high brittleness
3	0.6321	$M = -E$
4	0~0.6321	$-E < M < 0$, low brittleness
5	0	$M = 0$, ideal plasticity
6	<0	$M > 0$, strain hardening

increasing confining pressure, and from 5 MPa to 15 MPa, they decrease considerably more than they do from 25 MPa to 35 MPa. For B_2 and B_3 tend to decrease with increasing confining pressure, while their values increase at 35 MPa. B_4

increases with the confining pressure except at 35 MPa. B_5 decreases with confining pressure except at 25 MPa, and there are only small differences among the three decreasing values, which are not advantageous for the quantitative identification of rock brittleness. Above all, by comparative analysis, it is considered that B_1 and $B_2 \sim B_5$ can all be used to evaluate the change in rock brittleness with confining pressure, and the results of B_1 and $B_2 \sim B_4$ are good, while there are small differences in the results of $B_2 \sim B_5$.

The evaluation results of granite samples under 5 MPa with different loading modes are listed in Table 6. According to Table 6, B_1 and $B_1 \sim B_5$ all decrease during the compression tests. For B_1 and $B_2 \sim B_4$, their values during the unloading test are nearly 2 times those during the

TABLE 5: Calculation results of each index for marble under different confining pressures.

Confining pressure (MPa)	$\mathbf{B}_I \mathbf{B}_I \cdot \mathbf{B}_{II}$	Comparison of brittleness indices					Qualitative analysis of the test curve
		B_1	B_2	B_3	B_4	B_5	
5	0.152	0.76	0.26	1.13	0.36	0.66	Brittleness
15	0.110	0.39	0.21	0.83	0.47	0.65	Elasticity-plasticity
25	0.082	0.20	0.10	0.31	0.52	0.88	Elasticity-plasticity
35	0.078	0.19	0.13	0.45	0.48	0.63	Elasticity-plasticity

TABLE 6: Calculation results of each index of granite under different loading modes.

Loading mode	$\mathbf{B}_I \mathbf{B}_I \cdot \mathbf{B}_{II}$	Comparison of brittleness indices					Qualitative analysis of the test curve
		B_1	B_2	B_3	B_4	B_5	
Unloading	0.94	0.57	0.26	1.28	0.67	1.22	Brittleness
Compression	0.40	0.44	0.13	0.43	0.43	1.08	Strain softening

compression test, while there is only a small difference in B_1 and B_5 under the two loading modes. Based on the above analysis, \mathbf{B}_I and $B_1 \sim B_5$ all reflect the change in rock brittleness with the loading mode.

5. Conclusions

- (1) Taking the crack initiation strain ϵ_{ci} to characterize the ability of the rock to be compacted and the difference between the peak strain ϵ_c and crack initiation strain ϵ_{ci} ($\Delta \epsilon = \epsilon_c - \epsilon_{ci}$) to characterize the ability of crack propagation, the prepeak brittleness component ($\mathbf{B}_I = \epsilon_{ci}/\Delta \epsilon$) considering the crack initiation is established. If $\epsilon_{ci}/\Delta \epsilon$ is larger, the ability of the rock to maintain the crack compaction state is greater, and the prepeak brittleness is greater.
- (2) Based on the postpeak characteristic of a greater stress drop, the postpeak brittleness of rock is greater, and the postpeak brittleness component (\mathbf{B}_{II}) is established by the ratio of S/S_{Δ} . If S/S_{Δ} is larger, the stress drops faster after the peak, and the postpeak brittleness is greater.
- (3) A brittleness evaluation index based on the prepeak crack initiation and postpeak stress drop characteristics of the rock is established, and its expression is $\mathbf{B}_I = \mathbf{B}_I \cdot \mathbf{B}_{II}$.
- (4) The brittleness index \mathbf{B}_I can effectively reflect the effects of different confining pressures and loading modes on rock brittleness. Under the same conditions, the brittleness of rock during an unloading test is greater than that during a compressive loading test, and the brittleness of rock under low confining pressure is greater than that under a high confining pressure.

Data Availability

The data used to support the findings of this study are included within this article and are from Rock Mechanics Laboratory, State Key Laboratory of Geohazard Prevention

and Geoenvironment Protection, Chengdu University of Technology.

Conflicts of Interest

The authors declare that they have no conflicts of interest.

Authors' Contributions

Meiben Gao conceptualized, visualized, and wrote the article. Lubo Meng developed methodology. Tianbin Li supervised and collected fund. All authors have read and agreed to the published version of the manuscript.

Acknowledgments

This research was supported by the National Natural Science Foundation of China (U19A20111, 41772329, and 41230635) and the On-Campus Talent Introduction Project in Xihua University (Z201125).

References

- [1] S. P. Singh, "Brittleness and the mechanical winning of coal," *Mining Science and Technology*, vol. 3, no. 3, pp. 173–180, 1986.
- [2] S. Kahraman, "Correlation of TBM and drilling machine performances with rock brittleness," *Engineering Geology*, vol. 65, no. 4, pp. 269–283, 2002.
- [3] Q. M. Gong and J. Zhao, "Influence of rock brittleness on TBM penetration rate in Singapore granite," *Tunnelling and Underground Space Technology*, vol. 22, no. 3, pp. 317–324, 2007.
- [4] D. M. Jarvie, R. J. Hill, T. E. Ruble, and R. M. Pollastro, "Unconventional shale-gas systems: the Mississippian barnett shale of north-central Texas as one model for thermogenic shale-gas assessment," *AAPG Bulletin*, vol. 91, no. 4, pp. 475–499, 2007.
- [5] R. M. Holt, E. Fjær, J. F. Stenebråten, and O.-M. Nes, "Brittleness of shales: relevance to borehole collapse and hydraulic fracturing," *Journal of Petroleum Science and Engineering*, vol. 131, pp. 200–209, 2015.

- [6] C. Ai, J. Zhang, Y.-W. Li, J. Zeng, X.-L. Yang, and J.-G. Wang, "Estimation criteria for rock brittleness based on energy analysis during the rupturing process," *Rock Mechanics and Rock Engineering*, vol. 49, no. 12, pp. 4681–4698, 2016.
- [7] Y. Chen, Y. Jin, M. Chen, Z. Yi, and X. Zheng, "Quantitative evaluation of rock brittleness based on the energy dissipation principle, an application to type II mode crack," *Journal of Natural Gas Science and Engineering*, vol. 45, pp. 527–536, 2017.
- [8] S. Aligholi, G. R. Lashkaripour, and M. Ghafoori, "Strength/brittleness classification of igneous intact rocks based on basic physical and dynamic properties," *Rock Mechanics and Rock Engineering*, vol. 50, no. 1, pp. 45–65, 2016.
- [9] Y. Wang, X. Li, Y. Wu et al., "Research on relationship between crack initiation stress level and brittleness indices for brittle rocks," *Chinese Journal of Rock Mechanics and Engineering*, vol. 33, no. 2, pp. 264–275, 2014.
- [10] Y. Zhang, X.-T. Feng, C. Yang, Q. Han, Z. Wang, and R. Kong, "Evaluation method of rock brittleness under true triaxial stress states based on pre-peak deformation characteristic and post-peak energy evolution," *Rock Mechanics and Rock Engineering*, vol. 54, no. 3, pp. 1277–1291, 2021.
- [11] Z. K. Hou, C. H. Yang, X. Wei et al., "Experimental study on the brittle characteristics of Longmaxi formation shale," *Journal of China Coal Society*, vol. 41, no. 5, pp. 1188–1196, 2016.
- [12] R. Altindag, "Assessment of some brittleness indexes in rock-drilling efficiency," *Rock Mechanics and Rock Engineering*, vol. 43, no. 3, pp. 361–370, 2010.
- [13] A. Morley, "Notes and news," *The Lancet*, vol. 243, no. 6280, pp. 71–72, 1944.
- [14] M. Hetenyi, *Handbook of Experimental Stress Analysis*, Wiley, New York, NY, USA, 1950.
- [15] J. G. Ramsay, *The Folding and Fracturing of Rocks*, McGraw-Hill, London, UK, 1967.
- [16] L. Obert and W. I. Duvall, *Rock Mechanics and the Design of Structures in Rock*, John Wiley, New York, NY, USA, 1967.
- [17] B. Tarasov and Y. Potvin, "Universal criteria for rock brittleness estimation under triaxial compression," *International Journal of Rock Mechanics and Mining Sciences*, vol. 59, pp. 57–69, 2013.
- [18] Q. Li, M. Chen, Y. Jin, F. P. Wang, B. Hou, and B. Zhang, "Indoor evaluation method for shale brittleness and improvement," *Chinese Journal of Rock Mechanics and Engineering*, vol. 31, no. 8, pp. 1680–1685, 2012.
- [19] H. Honda and Y. Sanada, "Hardness of coal," *Fuel*, vol. 35, no. 4, pp. 451–460, 1956.
- [20] X. Jin, S. Shaw, J. A. Truax, and J. C. Roegiers, *A Practical Petrophysical Approach for Brittleness Prediction from Porosity and Sonic Logging in Shale Reservoirs*, Spe Atce, Dallas, London, 2014.
- [21] G. Chen, W. Jiang, X. Sun, C. Zhao, and C. A. Qin, "Quantitative evaluation of rock brittleness based on crack initiation stress and complete stress-strain curves," *Bulletin of Engineering Geology and the Environment*, vol. 78, no. 8, pp. 5919–5936, 2019.
- [22] F. Meng, H. Zhou, C. Zhang, R. Xu, and J. Lu, "Evaluation methodology of brittleness of rock based on post-peak stress-strain curves," *Rock Mechanics and Rock Engineering*, vol. 48, no. 5, pp. 1787–1805, 2015.
- [23] Z. K. Hou, C. H. Yang, L. Wang, and F. Xu, "Evaluation method of shale brittleness based on indoor experiments," *Journal of Northeastern University (Natural Science)*, vol. 37, no. 10, pp. 1496–1500, 2016.
- [24] S. Yagiz, "Assessment of brittleness using rock strength and density with punch penetration test," *Tunnelling and Underground Space Technology*, vol. 24, no. 1, pp. 66–74, 2009.
- [25] D. R. Reichmuth, "Point load testing of brittle materials to determine tensile strength and relative brittleness," in *Proceedings of the 9th US Symposium on Rock Mechanics (USRMS)*, Golden, Colorado, April 1967.
- [26] R. Rickman, M. Mullen, E. Petre, B. Grieser, and D. Kundert, "A practical use of shale petrophysics for stimulation design optimization: all shale plays are not clones of the Barnett shale," in *Proceedings of the SPE Annual Technical Conference & Exhibition*, Denver, CO, USA, September 2008.
- [27] D. F. Coates and R. C. Parsons, "Experimental criteria for classification of rock substances," *International Journal of Rock Mechanics and Mining Sciences & Geomechanics Abstracts*, vol. 3, no. 3, pp. 181–189, 1966.
- [28] V. Hajiabdolmajid and P. Kaiser, "Brittleness of rock and stability assessment in hard rock tunneling," *Tunnelling and Underground Space Technology*, vol. 18, no. 1, pp. 35–48, 2003.
- [29] X. G. Zhou, H. M. Liu, Y. T. Guo, L. Wang, Z. K. Hou, and P. Deng, "An evaluation method of brittleness characteristics of shale based on the unloading experiment," *Energies*, vol. 12, no. 9, pp. 1–24, 2019.
- [30] V. Hucka and B. Das, "Brittleness determination of rocks by different methods," *International Journal of Rock Mechanics and Mining Sciences & Geomechanics Abstracts*, vol. 11, no. 10, pp. 389–392, 1974.
- [31] E. A. George, *Brittle Failure of Rock Materials - Test Results and Constitutive Models*, pp. 123–128, A. A. Balkema, Rotterdam, Netherlands, 1995.
- [32] C. D. Martin, *The strength of massive Lac du Bonnet granite around underground openings*, University of Manitoba (Canada), Winnipeg, Canada, 1993.
- [33] Y. J. Xia, L. C. Li, C. A. Tang, X. Y. Li, S. Ma, and M. Li, "A new method to evaluate rock mass brittleness based on stress-strain curves of class I," *Rock Mechanics and Rock Engineering*, vol. 50, no. 5, pp. 1123–1139, 2017.
- [34] W. R. Wawersik and C. Fairhurst, "A study of brittle rock fracture in laboratory compression experiments," *International Journal of Rock Mechanics and Mining Sciences & Geomechanics Abstracts*, vol. 7, no. 5, pp. 561–575, 1970.
- [35] H. Zhou, F. Meng, C. Zhang, R. Xu, and J. Lu, "Quantitative evaluation of rock brittleness based on stress-strain curve," *Chinese Journal of Rock Mechanics and Engineering*, vol. 33, no. 6, pp. 1114–1122, 2014.
- [36] E. L. Liu and Z. J. Shen, "Study on brittleness of geomaterials," *Chinese Journal of Rock Mechanics and Engineering*, vol. 24, no. 19, pp. 3449–3453, 2005.
- [37] G. C. Shi, X. R. Ge, and Y. Lu, "Experimental study on coefficients of brittle stress drop of marble," *Chinese Journal of Rock Mechanics and Engineering*, vol. 25, no. 8, pp. 1625–1631, 2006.

Research Article

Numerical Investigation into the Distributions of Temperature and Stress around Wellbore during the Injection of Cryogenic Liquid Nitrogen into Hot Dry Rock Reservoir

Keda Ren ^{1,2} and Chengzheng Cai ^{1,2}

¹State Key Laboratory for Geomechanics and Deep Underground Engineering, China University of Mining and Technology, Xuzhou 221116, China

²School of Mechanics and Civil Engineering, China University of Mining and Technology, Xuzhou 221116, China

Correspondence should be addressed to Chengzheng Cai; caicz@cumt.edu.cn

Received 26 March 2021; Accepted 7 June 2021; Published 21 June 2021

Academic Editor: Guowen Xu

Copyright © 2021 Keda Ren and Chengzheng Cai. This is an open access article distributed under the Creative Commons Attribution License, which permits unrestricted use, distribution, and reproduction in any medium, provided the original work is properly cited.

Cryogenic liquid nitrogen fracturing is expected to provide an effective stimulation method for hot dry rock reservoirs to increase heat production. This paper establishes a three-dimensional model to calculate the distributions of temperature and stress of the reservoir rock when liquid nitrogen is injected into the wellbore. The sensitivity of different parameters and water fracturing to the stress state is studied. The results indicate that when liquid nitrogen is injected into the bottom of well, a huge heat exchange occurs on the rock surface, which generates great thermal stress on the fluid-solid interface, and the value of thermal stress exceeds the tensile strength of rock. For the effect of parameters, the primitive temperature of the rock has a significant impact on the value of maximum principal stress. The pressure drop and ambient pressure affect the thermal stress slightly. At the same time, a series of experiments are conducted to validate the effect of thermal stress induced by liquid nitrogen injection on the rock fracture. As the temperature rises, the shale samples are broken more severely at the action of thermal stress. Thus, the study of liquid nitrogen fracturing provides a scientific and effective method for geothermal exploitation.

1. Introduction

The hot dry rock (HDR) is green, low-carbon renewable energy in the reservoirs, which is regarded as an important alternative for conventional energy [1, 2]. HDR is defined as the high-temperature rock between 150 and 650°C in the deep subsurface. The common HDR includes granite, diorite, and gneiss [3]. The progress of geothermal mining from HDR is injecting cold water into reservoir and then returns to the ground through the production well. The cold water is heated by contacting the hot rock to achieve the purpose of extracting thermal energy. However, it is difficult to rely on the conductivity of natural fractures and the seepage ability of rocks to obtain economical heat flow due to the extremely low permeability of HDR reservoirs [4]. Because of extracting thermal energy, it not only needs to increase the permeability

of the reservoir, but also needs to increase the surface area of the fracture as much as possible. Therefore, stimulation methods should be adapted to increase the permeability [5–7].

At present, the main stimulation method of HDR resources is hydraulic fracturing, which has been widely used in increasing production of unconventional oil and gas [8–11]. However, the traditional hydraulic fracturing has some problems, such as the high fracture pressure, pore blockage caused by water sensitivity damage, and large water consumption [12–14]. In order to solve these problems, waterless stimulation methods are proposed. Compared to traditional hydraulic fracturing techniques, waterless fracturing is mainly unconstrained by water resources, which not only increases the fracturing fluid backdraft rate and reduces the damage of fracturing fluid to high-temperature reservoirs, but also reduces the waste of water resources.

As a method of waterless fracturing, cryogenic liquid nitrogen (LN) fracturing has its unique advantages in the process of fracturing HDR because of its extremely cryogenic property [15]. Cryogenic fracturing is defined as follows: huge temperature gradient causes local tensile stress to break rock, which is generated by the contact between cryogenic fluid and high-temperature rock [16]. The rock breakage due to thermal stress results from two aspects: thermal stress generated by the temperature gradient and adjacent minerals with different thermal expansion [17]. Thermal stress will cause microscopic damage inside the rock and increase the permeability, which is beneficial to extract heat from reservoir [18]. At the twentieth century, LN fracturing stimulation technology was used to increase production in the low-permeability Devonian shale, and favorable stimulation effects have been obtained [19]. For this technology, LN is injected into the target reservoir as a fracturing fluid instead of water-based fracturing fluid. In this case, thermal stress is generated to fracture rock due to cryogenic LN contact with high-temperature rock [20, 21]. During the LN fracturing, not only the macrofracture occurs in the rock, but also the intergranular breakage is generated in the microstructure, which promotes the appearance of complex fracture networks [22, 23].

Many previous investigations have been performed to study the rock damage due to LN cooling. Ren et al. [24] carried out experiments of LN thermal shock on coal sample and found that both the wave velocity and amplitude reduced sharply after LN treatment. The experimental results indicated that the internal structure damage occurred in the coal, which is beneficial for generating a fracture network to increase the permeability of rock. Cha et al. [16, 25] conducted cryogenic fracturing studies by injecting LN into concrete and sandstone samples. In this study, numerous microcracks were generated around the borehole due to the effect of thermal stress. This indicated that the LN entering the borehole can change the rock structure and induce fracture creation. Cai et al. [26, 27] investigated the change in the mechanical properties of rock samples after LN treatment. According to the experimental study, the obvious thermal fracture appeared on the rock surface, and the tensile strength and compressive strength of the rock were obviously weakened. This indicated that the treatment with LN has a great influence on the strength of rock samples. Yang et al. [28] conducted granite breakage experiment under different rock temperature and confining pressure. The experimental results showed that the fracture initiation pressure of granite was reduced and the microscopic pore structure was expanded after LN treatment. For the study of numerical simulation method, Yao et al. [29] simulated the LN stimulation process by the TOUGH2-EGS. The simulation results were also compared with experimental data. They found that the increase in reservoir seepage can be achieved by the injection of cryogenic fluid with high pressure. Cai et al. [30] simulated the transient fluid flow and heat transfer in the process of LN being injected into the downhole. The influence factors were also analyzed in this study. The results indicated that cryogenic LN can be generated in the downhole and has a great impact on

reservoir temperature. Kim et al. [21] studied the effect of rapid cooling on granite samples and found that the crack growth occurred in granite samples. Furthermore, the thermal stress distribution of rapid cooling was illustrated by a transient thermodynamic model. Zhang et al. [31] studied the granite damage under the impact of cryogenic LN by applying SEM methods. They found that the number of cracks and complexity of fracture network increased with the increase of temperature gradient. This indicated that the rock structure was damaged by LN and the temperature gradient was an important factor. Wu et al. [32, 33] conducted a set of experiments to investigate variations of physical and mechanical properties of granite, including density, wave velocity, strength, and elastic modulus. According to the experimental results, they pointed out that the destruction of granite is aggravated with the number of heating and cooling cycles increasing. Xi et al. [34] performed an experimental study into the effect of water cooling on mechanical properties of granite samples. The influence factor of rock initial temperature was considered in this study. They found that the thermal cracking occurred inside the rock, leading to the degradation of mechanical properties of granite samples. Huang et al. [22] conducted experiments to investigate the characteristics and mechanism of granite samples with LN jet. The results showed the damage of granite samples and the corresponding mechanical properties deteriorated obviously with the growth of primitive temperature. This suggested that the primitive rock temperature is an important factor determining the performances of rock breaking and cracking with cryogenic LN.

According to the literature review, most of studies focused on the mechanical properties deterioration of granite caused by thermal stress after LN treatment. The fracture characteristic of granite attributed to LN was discussed in laboratory investigation. However, the effect after injecting LN into the bottom of reservoir is still not clear. Hence, before the LN can be extensively implemented as a fracturing fluid instead of water-based fracturing fluid, many fundamental problems should be addressed to provide guidance on HDR stimulation. These problems included the heat transfer and the distribution of stress at the bottom of well during injecting LN into wellbore. The heat transfer contributes to the change of fracturing conditions, and the distribution of stress is directly related to the effect of fracturing.

This paper conducted a numerical simulation study on the heat transfer and the stress distributions of reservoir when LN was injected into the HDR reservoir. During the process of LN flowing into the wellbore, the tensile stress was generated due to the thermal stress and fluid pressure. The maximum principal stress was selected for analyzing the effect of thermal stress on rock failure, because the maximum principal stress can effectively determine the rock fracture when the tensile failure was generated in rock. The computational fluid dynamics (CFD) was used in the fluid region with standard $k-\epsilon$ turbulence model. The fluid-solid interface was adapted to conjugate heat transfer method. In the simulation, granite was adopted in solid region, which is common in HDR. Due to the large elastic modulus and small

deformation in granite, the thermoelastic mechanical model was adapted to calculate the stress and strain in solid region.

2. Geometric Model and Parameters

2.1. Physical Model. A three-dimensional model is established to study the heat transfer between LN and high-temperature rock and the stress distributions of rock during injecting LN into the reservoirs. The schematic of model is shown in Figure 1. This model is carried out by the thermal-hydraulic-mechanical coupling method in transient state. The geometric size of the model is shown in Table 1.

The model mainly includes two regions, the fluid region and the solid region. In the fluid region, the high-pressure LN is injected into a pipe and then flows through the annulus between the drill hole and pipe. The inlet and outlet boundary conditions of fluid region are set as pressure inlet and pressure outlet boundary condition, respectively. During LN flowing through the hole of rock, the heat of the rock will be transferred to the cryogenic fluid quickly, which results in rock temperature decreasing. Consequently, the thermal stress is generated in reservoir rock, leading to the variation of original stress distribution and even rock damage.

Based on the present analysis, the following assumptions are proposed: (1) the influence of seepage flow in rock is ignored in the calculation. (2) No deformation of rock is assumed in flow field computation. (3) The rock is assumed as a homogeneous, isotropic, and linearly elastic material. (4) The calculating process does not involve rock failure.

2.2. Numerical Model. For the progress of injecting fluid into the wellbore, the standard k- ε model is adapted for the simulation of turbulent flow because of the larger Reynolds number. Besides, the intense heat transfer will also occur between the cryogenic fluid and warm rock. Thus, the equations of mass conservation, momentum, and energy should be solved in the flow field.

Continuity equation:

$$\frac{\partial \rho_l}{\partial t} + \nabla(\rho_l \mathbf{v}) = 0, \quad (1)$$

where ρ_l is fluid density, kg/m³; t is time, s; and \mathbf{v} is velocity vector, m/s.

Momentum equation:

$$\frac{\partial}{\partial t}(\rho_l \mathbf{v}) + \nabla(\rho_l \mathbf{v} \cdot \mathbf{v}) = -\nabla p + \nabla(\mu \nabla \mathbf{v}) + \rho_l \mathbf{g}, \quad (2)$$

where p is pressure, Pa; μ is dynamic viscosity, N·s/m²; and \mathbf{g} is gravitational acceleration, m²/s.

Energy equation of fluid:

$$\frac{\partial}{\partial t}(\rho_l T_l) + \nabla(\rho_l \mathbf{v} T_l) = \nabla \left(\frac{\lambda_l}{c_p} \nabla T_l \right), \quad (3)$$

where T_l is fluid temperature, °C; λ_l is thermal conductivity of fluid, W/m·K; and c_p is specific heat at constant pressure, J/kg·K.

Turbulent kinetic energy equation:

$$\frac{\partial}{\partial t}(\rho_l k) + \frac{\partial}{\partial x_i}(\rho_l k v_i) = \frac{\partial}{\partial x_j} \left[\left(\mu + \frac{\mu_t}{\sigma_k} \right) \frac{\partial k}{\partial x_j} \right] + G_k - \rho_l \varepsilon - Y_M, \quad (4)$$

where k is turbulent kinetic energy, m²/s²; \mathbf{v} is the velocity, m/s; μ_t is turbulent viscosity, N·s/m²; σ_k is the turbulent Prandtl number for k ; G_k is generation of turbulence kinetic energy; ε is specific dissipation rate, J/kg·s; and Y_M is the contribution of the fluctuating dilatation.

Specific dissipation rate of turbulent kinetic energy:

$$\frac{\partial}{\partial t}(\rho_l \varepsilon) + \frac{\partial}{\partial x_i}(\rho_l \varepsilon v_i) = \frac{\partial}{\partial x_j} \left[\left(\mu + \frac{\mu_t}{\sigma_\varepsilon} \right) \frac{\partial \varepsilon}{\partial x_j} \right] + C_{1\varepsilon} \frac{\varepsilon}{k} G_k - C_{2\varepsilon} \rho_l \frac{\varepsilon^2}{k}, \quad (5)$$

where σ_ε is the turbulent Prandtl number for ε , and $C_{1\varepsilon}$ and $C_{2\varepsilon}$ are turbulent constant.

Besides, μ_t is defined as

$$\mu_t = \rho_l C_\mu \frac{k^2}{\varepsilon}, \quad (6)$$

where C_μ is turbulent constant. The empirical constants appearing in the above equations are given by the following values: $C_{1\varepsilon} = 1.44$, $C_{2\varepsilon} = 1.92$, $C_\mu = 0.09$, $\sigma_k = 1.0$, $\sigma_\varepsilon = 1.3$.

In the solid region, the heat conduction equation will be solved to calculate the temperature distribution. Furthermore, the stress state of rock owing to thermal stress is also considered in our model. The governing equations of the thermoelastic model are considered in the calculation.

The heat conduction of equation for rock:

$$\nabla(\lambda_s \nabla T_s) - c \rho_s \frac{\partial T_s}{\partial t} = 0, \quad (7)$$

where λ_s is thermal conductivity of rock, W/m·K; c is specific heat of rock, J/kg·K; ρ_s is rock density, kg/m³; and T_s is rock temperature, °C.

Physical equation:

$$\boldsymbol{\tau} = \frac{1}{2G} \left(\boldsymbol{\sigma} - \frac{\nu}{1+\nu} \Theta \mathbf{I} \right) + \alpha \Delta T_s \mathbf{I}, \quad (8)$$

where $\boldsymbol{\tau}$ is the strain of rock; G is shear modulus; $\boldsymbol{\sigma}$ is the total stress; ν is Poisson's ratio; Θ is the sum of the normal stresses; \mathbf{I} is the Kronecker delta; α is the coefficient thermal expansion, W/m·K; and ΔT_s is rock temperature difference, °C.

Equilibrium equation:

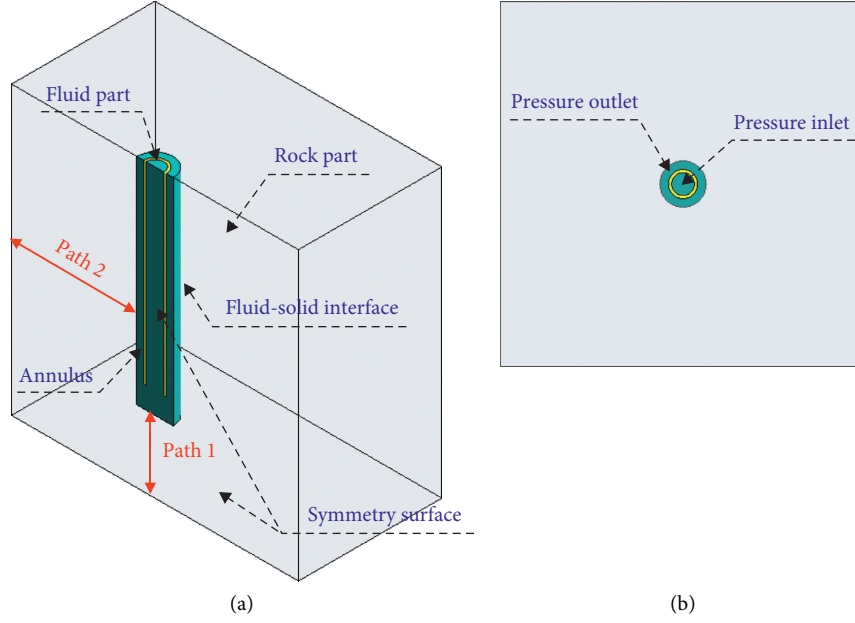


FIGURE 1: The geometry model of computation zones.

TABLE 1: Geometric parameters of the model shown in Figure 1.

Pipe inner diameter (mm)	Pipe outer diameter (mm)	Pipe length (mm)	Wellbore diameter (mm)	Well depth (mm)	Model
25.4	31.8	270	50.8	300	400 × 400 × 400 mm ³

$$\nabla \sigma + \rho_s \mathbf{g} = 0, \quad (9)$$

where ρ_s is rock density.

The strain-displacement relation is

$$\boldsymbol{\tau} = \frac{1}{2} (\nabla \mathbf{u} + \mathbf{u} \nabla), \quad (10)$$

where \mathbf{u} is the displacement.

2.3. Boundary Conditions. To analyze the temperature and stress distributions of the rock during the process of injecting LN into the wellbore, the simulation parameters are set as in Table 2. Besides, it is assumed that the fluid region is initially filled with gaseous nitrogen (GN). During the simulation, the GN and rock are set to the same initial temperature. The LN is injected from the pipe inlet (i.e., inlet boundary condition), and its temperature is regarded as the injection temperature. In the solid region, the geological conditions of wellbore Newberry are referenced. It is assumed that the wellbore is located at the subsurface of 1.5 km depths, whose temperature is 150°C. The maximum principal stress is vertical with a gradient of 24.1 MPa/km, and the minimum principal stress is 14.9 MPa/km. Therefore, the front, left, and bottom surface of the model are set as displacement boundary conditions, in which the normal displacement is zero. Both the right and backside surfaces are

set as stress boundary conditions, and their value is 22.35 MPa. The upper surface is set as stress boundary condition with the value of 36.15 MPa [35, 36].

In addition, the surface contacted the fluid region, and the solid region is set as the fluid-solid interface, which causes a large amount of heat exchange. The conjugate heat transfer method is used to simulate the heat transfer in the fluid-solid interface. Under conjugated boundary conditions, the temperature and the heat flux of the fluid and solid are equal, respectively. The corresponding mathematical expressions are as follows:

$$\begin{aligned} T_l|_{\text{wall}} &= T_s|_{\text{wall}}, \\ \lambda_l \frac{\partial T_l}{\partial n}|_{\text{wall}} &= \lambda_s \frac{\partial T_s}{\partial n}|_{\text{wall}}, \end{aligned} \quad (11)$$

where the T_l and T_s are the fluid temperature and the solid temperature at the solid-fluid interface, respectively; λ_l is the thermal conductivity of fluid; λ_s is the solid's thermal conductivity; and n is the common normal direction of the solid-fluid interface.

2.4. Material Parameters. In the progress of the simulation, the detailed modeling parameters used are shown in Table 3. It is assumed that the parameters, including density, specific heat, thermal conductivity, and viscosity of LN, are

TABLE 2: Simulation parameters of fluid region.

Inlet pressure (MPa)	Outlet pressure (MPa)	Initial temperature (°C)	Injection temperature
25	20	150	-173°C

TABLE 3: Material parameters.

	LN	Granite	
Density	806.08 kg m ⁻³	Density	2700 kg/m ³
Specific heat	2041.50 J (kg·K)	Elastic model	43.20 GPa
Thermal conductivity	0.15 W (m·K)	Poisson's ratio	0.22
Viscosity	1.61 × 10 ⁻⁴ kg (m·s)		

unchanged in simulation progress. For injecting LN into the wellbore, the injection temperature is set as -173°C. In addition, the granite properties in calculation are referred to in the experimental data by Park [37]. Regarding the thermal-physical properties of granite, the fitting equations of specific heat, thermal conductivity, and thermal expansion with temperature are adopted in the calculation based on previous studies [37, 38].

The specific heat of granite:

$$C_s(T_s) = -3.319 \times 10^{-3} T_s^2 + 1.889 T_s + 699.4 \quad (-180^\circ\text{C} \leq T_s \leq 300^\circ\text{C}), \quad (12)$$

where C_s is rock specific heat, J/kg·K.

The thermal conductivity coefficient of granite:

$$\lambda_s(T_s) = -2.691 \times 10^{-3} T_s + 2.6038 \quad (-180^\circ\text{C} \leq T_s \leq 300^\circ\text{C}), \quad (13)$$

where λ_s is thermal conductivity coefficient of rock, W/m·K.

The thermal expansion coefficient of granite:

$$\alpha(T_s) = \begin{cases} (0.0448 T_s + 2.294) \times 10^{-6} & (0^\circ\text{C} < T_s \leq 300^\circ\text{C}), \\ 2.294 \times 10^{-6} & (-180^\circ\text{C} \leq T_s \leq 0^\circ\text{C}), \end{cases} \quad (14)$$

where α_s is thermal expansion coefficient of rock.

3. Results and Discussion

3.1. Mesh Independence and Time Step Selection. To ensure the accuracy of the simulation, mesh independence is validated with four different cell number cases (see Table 4), in which the primitive rock temperature is set as 150°C, the time step is set as 0.2 s, and other parameters remain unchanged. The point below the bottom surface of wellbore 1 mm is employed as the monitoring point. Variation of temperature against grid number is plotted in the logarithmic coordinate shown in Figure 2(a). Temperature just changes by 0.25% as the grid number increases from 2071302 to 2250028; thus, Case 3 is adopted in the following calculation.

TABLE 4: Mesh scheme.

Mesh study case	Case 1	Case 2	Case 3	Case 4
Grid number	1452566	1757972	2071302	2250028

In the meantime, time step is also an important influencing parameter in transient calculation. Different time steps, including 0.05 s, 0.1 s, 0.2 s, 0.5 s, and 1 s, are computed to verify that the time step is independent of simulation results. As shown in Figure 2(b), when time step is less than 0.1 s, the temperature of the monitoring point changes slightly; however, it increases sharply when time step is beyond 0.1 s. Considering computational precision and efficiency, 0.1 s is selected as the optimal time step for the computation in later simulation.

3.2. Flow Field Analysis. The fluid flow numerical solution is performed based on the CFD code of Fluent with coupled algorithm. It can simulate flow field and heat transfer by coupling mass conservation, momentum, energy, and heat conductivity equations. The computation results indicate that the parameters of pressure and velocity change slightly with time during the process of computation. Thus, the steady state flow is analyzed in this section. Figure 3 shows the contours of velocity and static pressure in flow field.

As shown in Figure 3(a), the velocity of LN increases near the outlet of tube and then decreases sharply at the bottom of the wellbore. Besides, at the center point of the bottom of well, the velocity of the LN drops to zero due to the boundary effect, and the hydrostatic pressure increases greatly at the same time as shown in Figure 3(b). Then, the LN flows diffusively around the stagnation point at the action of hydrostatic pressure. Moreover, there is a low velocity area near the pipe outlet due to the effect of fluid turbulence, which results in a lower pressure in the near area.

3.3. Rock Temperature Distribution. The temperature contours in the symmetry plane of model at different times are shown in Figure 4. The primitive rock temperature is set as 150°C in this case. At the action of pressure, the LN flows into the bottom of well through the pipe, which results in a lower temperature in fluid-solid interface at 0.1 s. The cooled-region of rock constantly increases with time going by. Because the cooled-region is circular in rock, the radius of cooled-region is chosen to compare the effect of heat transfer at different conditions. Specifically, it is expressed by the distance along path 1 and path 2 (see Figure 1). Path 1 is the line along the axial direction of rock center at the bottom of well, and path 2 is 100 mm above the bottom of well along the radial direction in rock. The temperature distribution at different times along path 1 and path 2 is shown in Figure 5. It is noted that the initial point temperature of path 1 and path 2 quickly drops to -156.3°C and -136.6°C, respectively, as soon as LN connects to rock for 0.1 s. However, both the cooling distances of path 1 and path 2 are about 24 mm at 20 s. During the process of injecting LN into wellbore, the fluid comes into contact with the rock of wellbore bottom

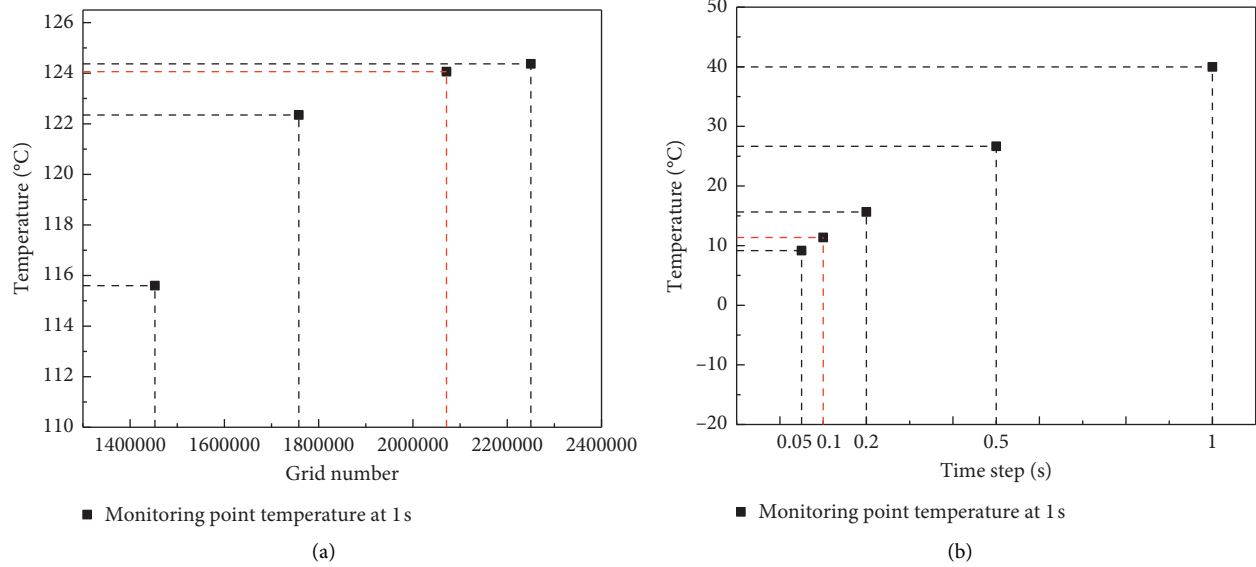


FIGURE 2: Sensitivity of mesh and time step: (a) the monitoring point temperature at 1 s with different grid number; (b) the monitoring point temperature at 1 s with different time step.

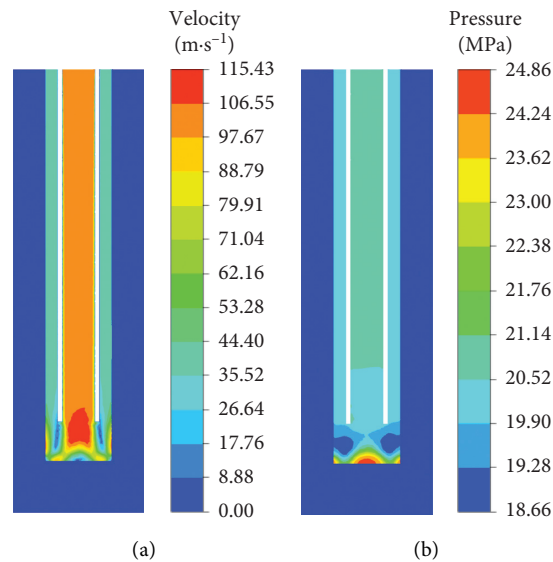


FIGURE 3: The contours of velocity and pressure in flow field of LN under steady state.

first, which results in a low temperature region at the bottom rather than the side area at 0.1 s. However, with the high-speed flow of the LN, the temperature of solid-fluid interface will remain the same, and the distance of cooled-region perpendicular to the solid-fluid interface will also be similar.

For the inner region of rock, its cooled-region is constantly increasing, but the growth trend in cooled-region becomes slower and slower. Based on (10) and (11), we could conclude that, with rock temperature rising, the thermal conductivity drops, while the specific heat increases. In this case, more heat is required to be carried away to cool the rock. As a result, the growth of cooled-region in inner rock will be slowed down.

3.4. Maximum Principal Stress Analysis. The thermal stress will be generated due to the rock temperature decreasing. Therefore, the stress state in rock would be changed with the effects of thermal stress and fluid pressure. A vertical plane 1 which is 100 mm above the downhole is chosen to show the maximum principal stress contour of rock at different times (see Figure 6). Here, the positive and negative values represent the tensile and compressive stresses, respectively. The thermal stress is generated by the temperature gradient inside the rock with cryogenic LN flowing along the surface of the rock. In addition, it can be found that tensile stress zone increases with time going by due to the inside rock cooling down. This shows that

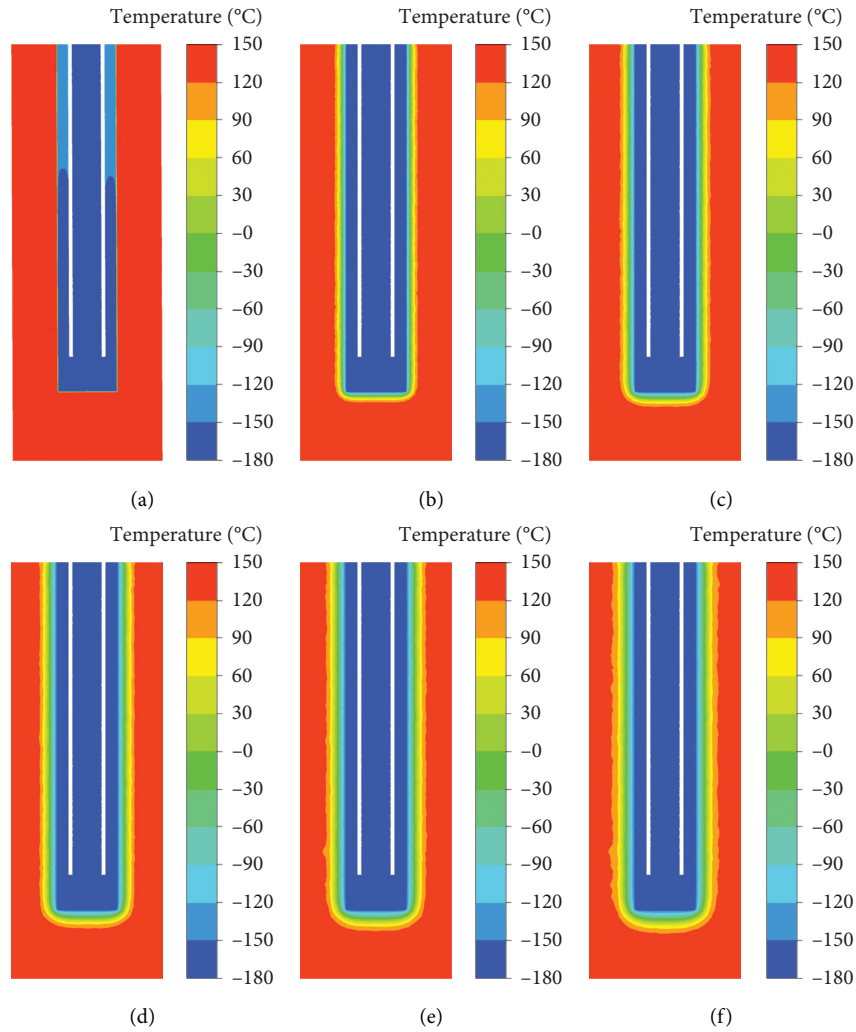


FIGURE 4: The temperature contours in the symmetry plane of model at different times: (a) 0.1 s; (b) 20 s; (c) 40 s; (d) 60 s; (e) 80 s; (f) 100 s.

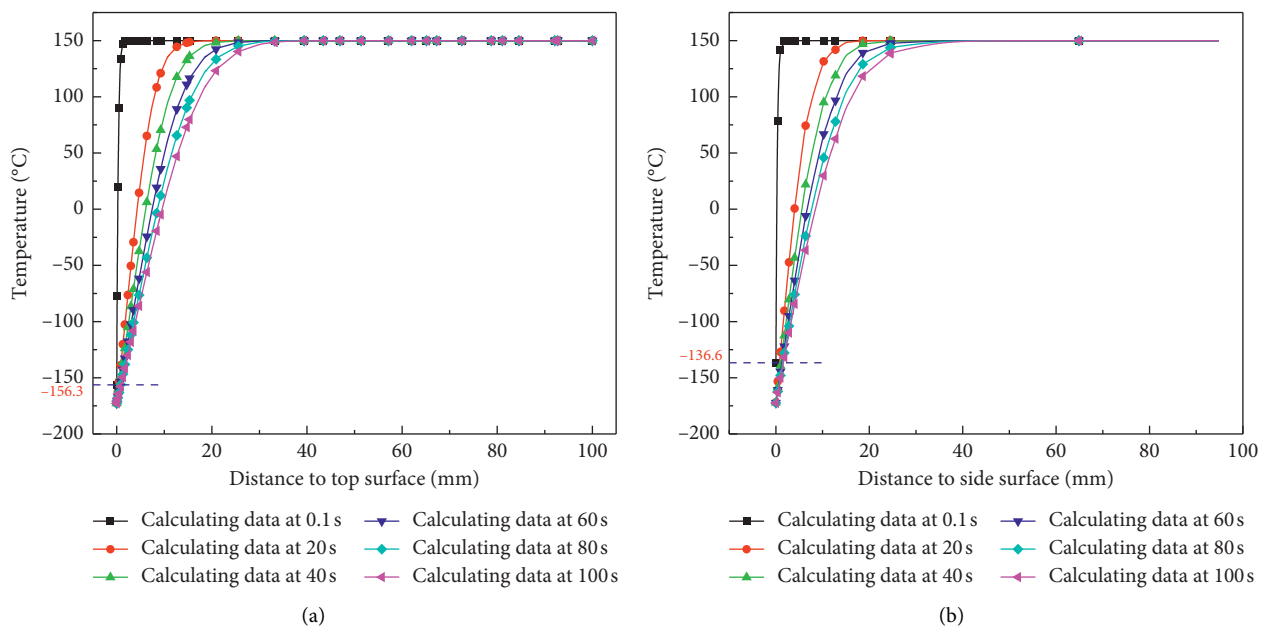


FIGURE 5: Temperature distribution at different times along path 1 and path 2, respectively: (a) path 1; (b) path 2.

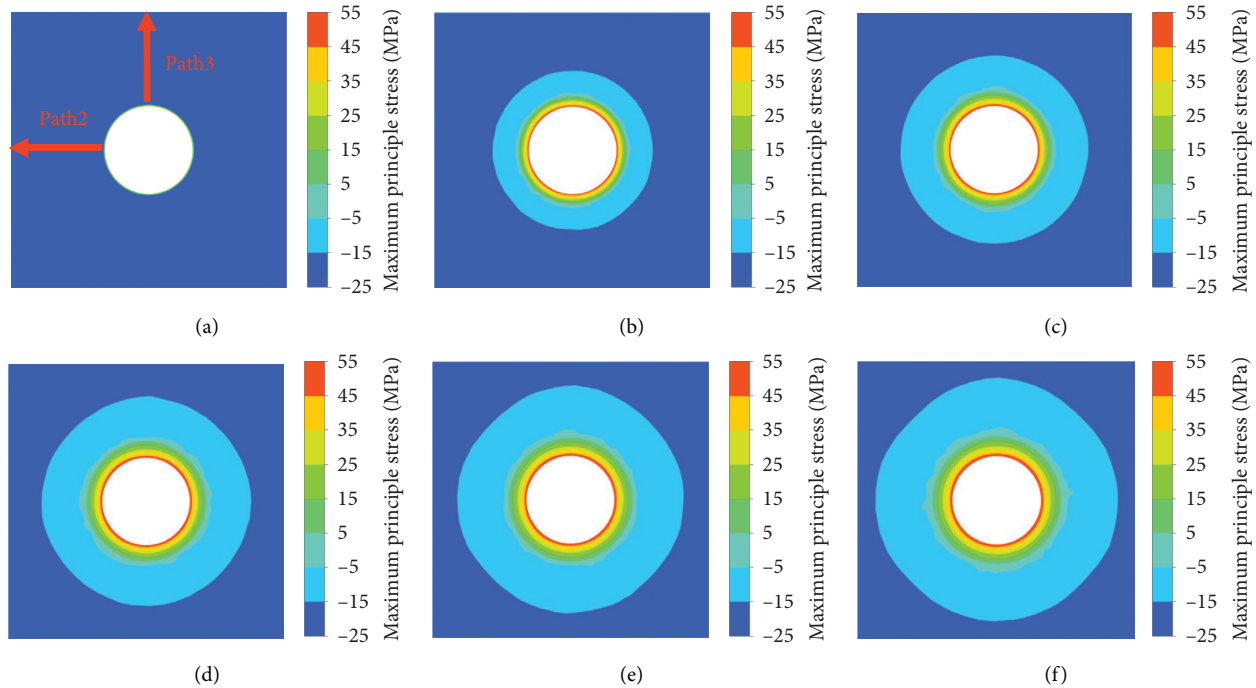


FIGURE 6: The maximum principal stress contours of rock plane 1 at different times: (a) 0.1 s; (b) 20 s; (c) 40 s; (d) 60 s; (e) 80 s; (f) 100 s.

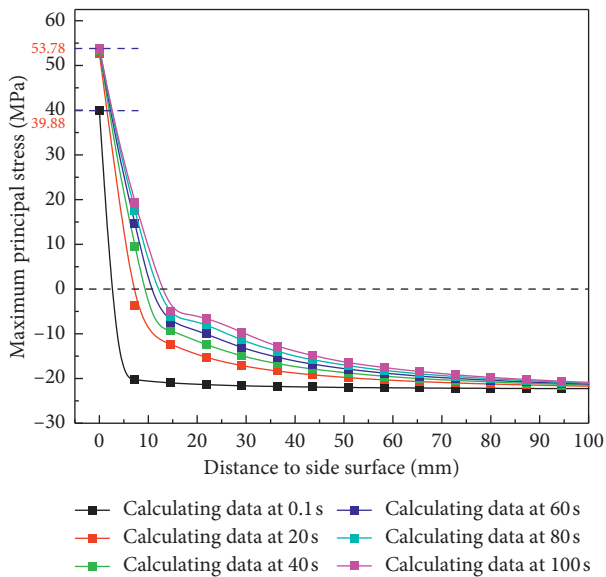


FIGURE 7: The maximum stress in hot rock along path 2 at different times.

injecting LN can change the original stress state and the fracturing environment.

Figure 7 illustrates the maximum principal stress distributions at different times along path 2. There are small changes for maximum principal stress values at different times except 0.1 s. This is because the surface temperature of rock is in unsteady state at 0.1 s. This also indicates that the maximum principal stress is gradually increasing during the period of LN contact with rock surface. The value of tensile stress generated at 100 s is much greater

than the tensile strength of granite, which shows that it is feasible to break rock by injecting LN. Besides, the tensile stress zone gradually increases with time going by. This is favorable for the rock to form complex fracture networks [18].

3.5. Parameter Analysis. Figure 8 shows the maximum principal stress along path 2 with different primitive rock temperature at 20 s. The results indicate that, with primitive rock temperature rising, the value of maximum principal stress also increases along path 2. The maximum principal value of stress is about 154.55 MPa for the rock with the primitive temperature of 300°C, which is much greater than the value with the primitive temperature of 150°C. The reason is that larger temperature difference is generated on rock surface with the primitive rock temperature rising, and it also leads to much larger deformation correspondingly. In addition, when the primitive temperature increases from 150°C to 300°C, the zone of tensile stress zone increases due to the larger maximum principal stress being generated on the rock surface, which is beneficial to the cracking and breaking of rock.

The difference between the inlet and ambient pressure is defined as the pressure drop. Figure 9 shows the maximum principal stress along path 2 with different pressure drop at 20 s. The results indicate that the distributions of maximum principal stress are hardly affected by the inlet pressure with the same ambient pressure. The reason is that the thermal conductivity and the heat transfer rate of rock are limited; the rock cooling performance cannot be enhanced efficiently by improving the inlet pressure. When the ambient pressure of reservoir has not been changed, the thermal stress induced by rock cooling is the main factor on the rock stress distribution.

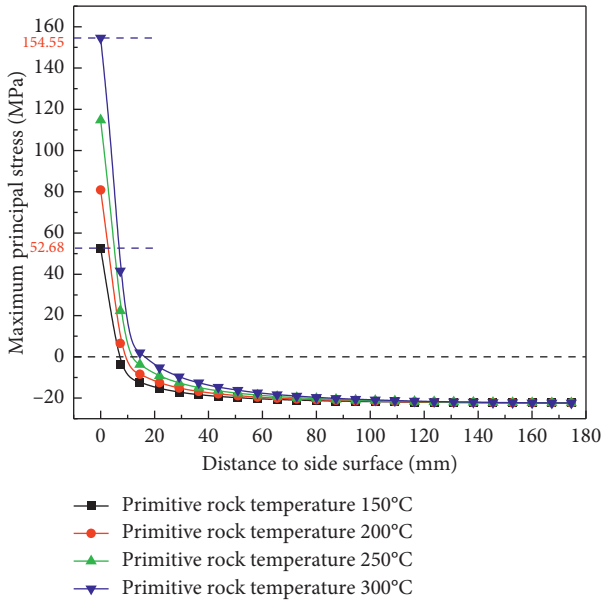


FIGURE 8: The maximum principal stress in rock along path 2 with different primitive temperature of rock at 20 s.

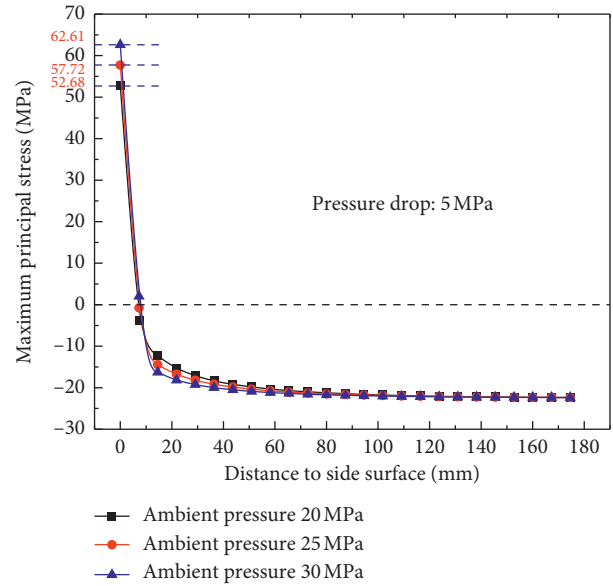


FIGURE 10: The maximum principal stress in rock along path 2 with different inlet pressure at 20 s.

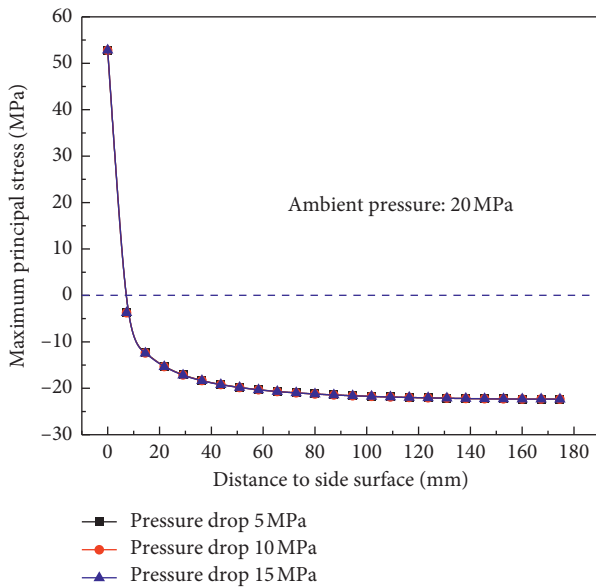


FIGURE 9: The maximum principal stress along path 2 with different pressure drop at 20 s.

The ambient pressure is also a significant factor on rock fracturing. The maximum principal stress along path 2 with different ambient pressure is shown in Figure 10. Similarly, there is a small change in the distribution of stress along path 2. Because the inlet pressure also hardly affects the rock cooling performance during the LN flowing along wellbore, the thermal stress of rock almost remains unchanged. The value of maximum principal stress is slightly increased due to the effect of fluid pressure.

To study the influence of different stress boundary on stress distribution, we calculate the maximum principal stress with different stress boundary as shown in Figure 11. It

indicates that tensile stress will appear on the coupled surface when stresses on both sides of the plane are equal, and the maximum principal stresses along the circumference are similar. When the stresses on both sides are unequal, the maximum principal stress on the coupled surface of wellbore will change. With the increasing of σ_H , the maximum principal stress area in the axial direction will decrease gradually, and the maximum principal stress near wellbore along the radial direction also decreases at the same time. The greater the difference is, the more obvious the trend will be. Figure 12 illustrates the value of maximum principal stress in rock along path 3 under different stress boundary. It could be clearly seen that maximum principal stress near coupled interface decreases with σ_H improving. Thus, it could be reasonably predicted that the rock will be fractured toward the direction of larger in situ stress when LN flows into wellbore.

To analyze the effect of thermal stress induced by LN cooling, the water cooling is also considered under the same conditions. The physical properties of water are set as follows: density is 998.2 kg/m^3 , specific heat is $4182 \text{ J/(kg}\cdot\text{K)}$, thermal conductivity is $0.6 \text{ W/(m}\cdot\text{K)}$, and viscosity is $0.001003 \text{ kg/(m}\cdot\text{s)}$. When the stress caused by injecting water into the reservoirs is calculated, the inlet temperature is set as 25°C . Figure 13 shows the maximum principal stress along path 2 with LN and water flowing into wellbore at 100 s, respectively. In this case, the maximum principal stress in the side surface of rock is about 21.02 MPa at 100 s with the water flowing into wellbore, which is about 39.90% caused by LN under the same conditions. This indicated that, due to the extremely cryogenic characteristic, LN will generate greater tensile stress on the rock surface during the progress of flowing into wellbore compared with water. It is beneficial to reduce the injection pressure.

In order to study the effect of inlet pressure on stress distribution around wellbore as water flows into the bottom of the wellbore, the maximum principal stress of wellbore

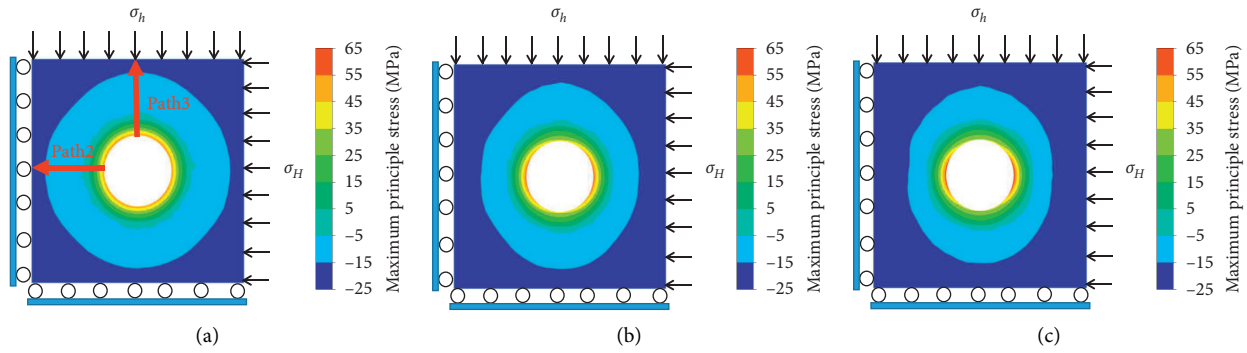


FIGURE 11: Maximum principal stress contours of hot rock plane 1 with different stress boundary at 100 s: (a) $\sigma_H = 22.35$ MPa, $\sigma_h = 22.35$ MPa; (b) $\sigma_H = 27.35$ MPa, $\sigma_h = 22.35$ MPa; (c) $\sigma_H = 22.35$ MPa, $\sigma_h = 32.35$ MPa.

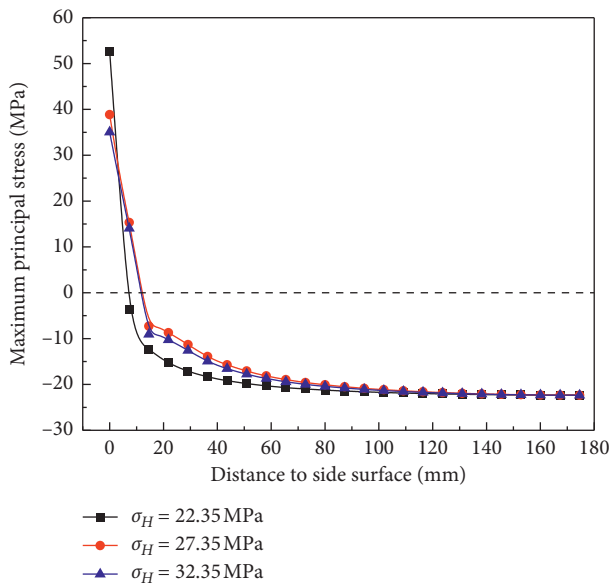


FIGURE 12: The maximum principal stress in rock along path 3 with different stress boundary at 100 s.

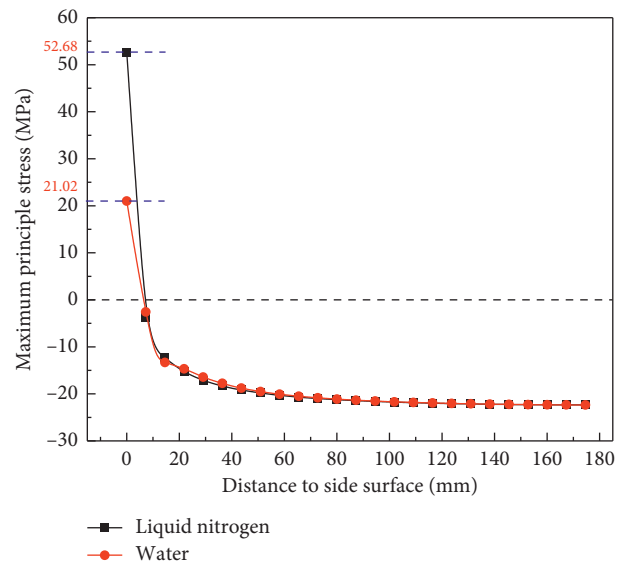


FIGURE 13: The maximum principal stress in rock along path 2 with different working fluid at 100 s.

surface at 100 s under the same pressure drop is calculated. Figure 14 shows the maximum principal stress in rock with different inlet pressure at 100 s. It is noted that there is an obvious linear relationship between the water inlet pressure and the maximum principal stress. The fitting expression is

$$\sigma = P - 3.69, \tag{15}$$

Where P is inlet pressure and σ is maximum principal stress.

In addition, the value of maximum principal stress is about 50.65 MPa with the inlet pressure of 55 MPa, which is similar to the value caused by LN flowing at 25 MPa under the same conditions. This shows that LN injection into the wellbore for fracturing operations can effectively reduce the inlet pressure due to its cryogenic properties compared with fracturing by water.

The variation of stress values due to water injection under different in situ stress conditions was analyzed. Figure 15 shows the values of maximum principal stress at the surface of wellbore with the relationship of σ_H . It indicated that as σ_H increases, the value of maximum principal stress decreases at

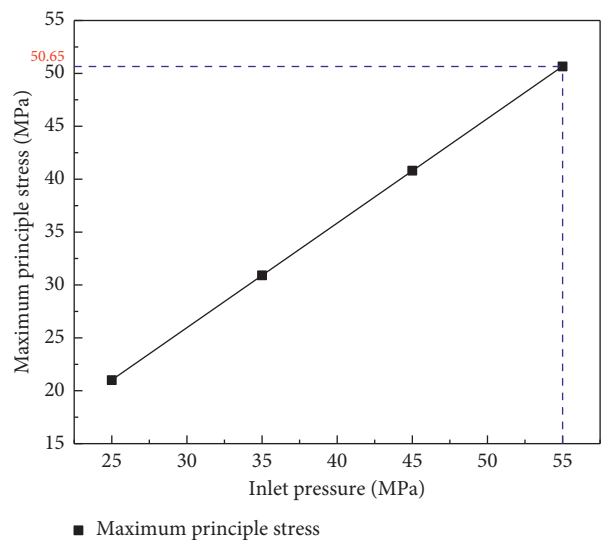


FIGURE 14: The maximum principal stress in rock with different water inlet pressure at 100 s.

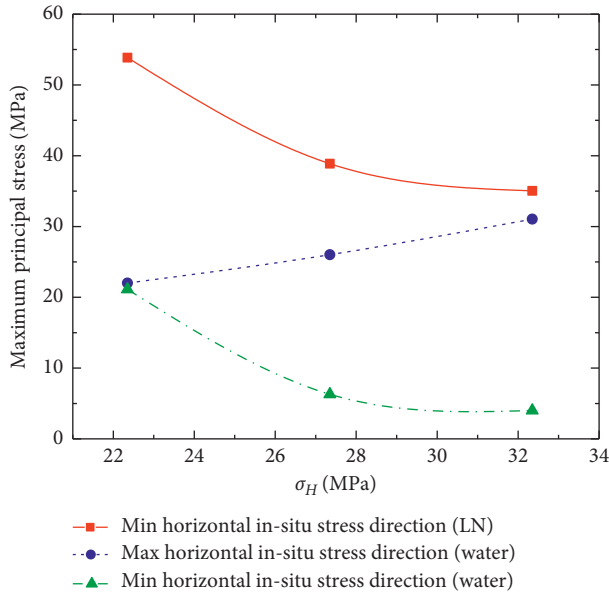


FIGURE 15: Maximum principal stress at the surface of the wellbore under different in situ stress conditions after LN and water injection for 100 s.

the surface of wellbore in the direction of minimum horizontal in situ stress, which is the same trend as the effect of LN injection on the values of maximum principal stress. However, when σ_H is 32.35 MPa, the maximum principal stress in the direction of maximum horizontal in situ stress is about 31.04 MPa generated by the water injection, which is lower than the stress value of 35.04 MPa at the direction of minimum horizontal in situ stress by the injected LN. It can be concluded that the tensile damage could be generated in the direction of minimum horizontal in situ stress by the LN injection during the fracture process by injecting water and LN at the same inlet pressure. This is mainly due to the fact that the LN injection process generates a huge thermal stress in the surface of wellbore. The value of thermal stress is not affected by the in situ stress distribution, so the thermal cracks are formed under the thermal stress, which is beneficial to the cracks expansion. Based on this, a more complex fracture network is formed in the reservoir. It has been demonstrated that the main fracture direction of rock samples after LN fracturing does not extend exactly in the direction of the maximum principal stress [39].

4. Conclusion

In this paper, the heat transfer and stress state during injecting LN into HDR reservoirs are analyzed based on a 3D thermal-hydraulic-mechanical coupling numerical model. The parameters' sensitivity is analyzed in detail, and the injection of water under the same conditions is also considered. Finally, a set of experiments is conducted to validate the effect of thermal stress on the rock. The main conclusions of this paper are as follows:

- (1) The LN injected into the wellbore causes the rocks around the wellbore to cool down. As time passes by,

the increasing amplitude of cooled-region is weakened. During this progress, the great tensile stress that exceeds the tensile strength of granite is generated around the wellbore due to the action of thermal stress and fluid pressure.

- (2) The primitive temperature of the reservoir has a significant impact on the stress distributions around the wellbore during LN injecting. With the growth of the primitive temperature, the thermal stress value around wellbore becomes larger. The inlet pressure and the ambient pressure have little effect on the thermal stress generated by LN cooling.
- (3) The in situ stresses affect the stress distribution during LN fracturing. Under the unequal in situ stress in different directions, the value of maximum principal stress is larger in the direction with larger in situ stress; i.e., the rock has a tendency to break in the direction of the larger in situ stress value.
- (4) Compared with the injection of LN, the value of thermal stress around the wellbore caused by water injection is reduced under the same conditions. The thermal stress value around the wellbore during LN injecting with injection pressure of 25 MPa is similar to that during water injecting with injection pressure of 55 MPa. This means that LN fracturing can reduce the injection pressure effectively and achieve a better fracturing effect.

Data Availability

The data used to support the findings of this study are available from the corresponding author upon request.

Conflicts of Interest

The authors declare no conflicts of interest.

Authors' Contributions

Chengzheng Cai contributed to conceptualization. Keda Ren participated in data curation and reviewed and edited the manuscript. Both authors were responsible for methodology, software, supervision, and original draft preparation.

Acknowledgments

This research was funded by the National Key R&D Program of China (2020YFA0711800), the Assistance Program for Future Outstanding Talents of China University of Mining and Technology (2020WLJCRCZL010), the Postgraduate Research and Practice Innovation Program of Jiangsu Province (KYCX20_2042), and the National Natural Science Foundation of China (51604263).

References

- [1] Z. Huang, S. Zhang, and R. Yang, "A review of liquid nitrogen fracturing technology," *Fuel*, vol. 266, Article ID 117040, 2020.

- [2] E. Barbier, "Geothermal energy technology and current status: an overview," *Renewable and Sustainable Energy Reviews*, vol. 6, no. 1, pp. 3–65, 2002.
- [3] R. Hashizume, "Study of hot dry rock geothermal power plant in Kansai area," in *Proceedings of the World Geothermal Congress*, Florence, Italy, May, 1995.
- [4] D. M. Jarvie, R. J. Hill, T. E. Ruble et al., "Unconventional shale-gas systems: the Mississippian Barnett Shale of north-central Texas as one model for thermogenic shale-gas assessment," *AAPG Bulletin*, vol. 91, no. 4, pp. 475–499, 2007.
- [5] Q. Li, H. Xing, J. Liu et al., "A review on hydraulic fracturing of unconventional reservoir," *Petroleum*, vol. 1, no. 1, pp. 8–15, 2015.
- [6] G. Li, Z. Huang, S. Tian et al., "Research and application of water jet technology in well completion and stimulation in China," *Petroleum Science*, vol. 7, no. 2, pp. 239–244, 2010.
- [7] D. Wang, Y. Dong, D. Sun et al., "A three-dimensional numerical study of hydraulic fracturing with degradable diverting materials via CZM-based FEM," *Engineering Fracture Mechanics*, vol. 237, Article ID 107251, 2020.
- [8] C. T. Montgomery and M. B. Smith, "Hydraulic fracturing: history of an enduring technology," *Journal of Petroleum Technology*, vol. 62, no. 12, pp. 26–40, 2010.
- [9] W. Kumari, P. G. Ranjith, M. Perera et al., "Hydraulic fracturing under high temperature and pressure conditions with micro CT applications: geothermal energy from hot dry rocks," *Fuel*, vol. 230, pp. 138–154, 2018.
- [10] Y. M. Lekontsev and P. V. Sazhin, "Application of the directional hydraulic fracturing at Berezovskaya Mine," *Journal of Mining Science*, vol. 44, no. 3, 2008.
- [11] D. Wang, S. Zlotnik, P. Dz et al., "A numerical study on hydraulic fracturing problems via the Proper generalized decomposition method," *Computer Modeling in Engineering & Sciences*, vol. 122, no. 2, pp. 703–720, 2020.
- [12] G. S. Penny, M. W. Conway, and R. A. Schraufnagel, "The evaluation of proppant transport and cleanup of foamed fluids used in hydraulic fracturing of shallow, water-sensitive reservoirs," in *Proceedings of the Society of Petroleum Engineers Eastern Regional Meeting*, Pittsburgh, PA, USA, November, 1993.
- [13] D. J. Rozell and S. J. Reaven, "Water pollution risk associated with natural gas extraction from the Marcellus Shale," *Risk Analysis: An International Journal*, vol. 32, no. 8, pp. 1382–1393, 2012.
- [14] K. B. Gregory, R. D. Vidic, and D. A. Dzombak, "Water management challenges associated with the production of shale gas by hydraulic fracturing," *Elements*, vol. 7, no. 3, pp. 181–186, 2011.
- [15] L. Wang, B. Yao, M. Cha et al., "Waterless fracturing technologies for unconventional reservoirs-opportunities for liquid nitrogen," *Journal of Natural Gas Ence & Engineering*, vol. 35, pp. 160–174, 2016.
- [16] M. Cha, X. Yin, T. Kneafsey et al., "Cryogenic fracturing for reservoir stimulation-Laboratory studies," *Journal of Petroleum Science and Engineering*, vol. 124, pp. 436–450, 2014.
- [17] H. F. Wang, B. P. Bonner, S. R. Carlson et al., "Thermal stress cracking in granite," *Journal of Geophysical Research Solid Earth*, vol. 94, no. B2, 1989.
- [18] F. Gao, C. Cai, and Y. Yang, "Experimental research on rock fracture failure characteristics under liquid nitrogen cooling conditions," *Results in Physics*, vol. 9, pp. 252–262, 2018.
- [19] S. R. Grundmann, G. D. Rodvelt, G. A. Dials et al., *Cryogenic Nitrogen as a Hydraulic Fracturing Fluid in the Devonian Shale*, SPE Eastern Regional Meeting, Society of Petroleum Engineers, Pittsburgh, PA, USA, 1998.
- [20] K. M. Kim and J. Kemeny, *Effect of Thermal Shock and Rapid Unloading on Mechanical Rock Properties*, American Rock Mechanics Association, Houston, TX, USA, 2009.
- [21] K. Kim, J. Kemeny, and M. Nickerson, "Effect of rapid thermal cooling on mechanical rock properties," *Rock Mechanics and Rock Engineering*, vol. 47, no. 6, pp. 2005–2019, 2014.
- [22] Z. Huang, X. Wu, R. Li et al., "Mechanism of drilling rate improvement using high-pressure liquid nitrogen jet," *Petroleum Exploration and Development*, vol. 46, no. 4, pp. 810–818, 2019.
- [23] L. Zhang, S. Lu, C. Zhang et al., "Effect of cyclic hot/cold shock treatment on the permeability characteristics of bituminous coal under different temperature gradients," *Journal of Natural Gas Science and Engineering*, vol. 75, Article ID 103121, 2020.
- [24] S. Ren, Z. Fan, L. Zhang et al., "Mechanisms and experimental study OF thermal-shock effect ON coal-rock using liquid nitrogen," *Chinese Journal of Rock Mechanics & Engineering*, vol. 32, pp. 3790–3794, 2013.
- [25] M. Cha, N. B. Alqahtani, X. Yin et al., "Laboratory system for studying cryogenic thermal rock fracturing for well stimulation," *Journal of Petroleum Science and Engineering*, vol. 156, pp. 780–789, 2017.
- [26] C. Cai, G. Li, Z. Huang et al., "Experimental study of the effect of liquid nitrogen cooling on rock pore structure," *Journal of Natural Gas Science and Engineering*, vol. 21, pp. 507–517, 2014.
- [27] C. Cai, G. Li, Z. Huang et al., "Experiment of coal damage due to super-cooling with liquid nitrogen," *Journal of Natural Gas Science and Engineering*, vol. 22, pp. 42–48, 2015.
- [28] R. Yang, Z. Huang, Y. Shi et al., "Laboratory investigation on cryogenic fracturing of hot dry rock under triaxial-confining stresses," *Geothermics*, vol. 79, pp. 46–60, 2019.
- [29] B. Yao, L. Wang, X. Yin et al., "Numerical modeling of cryogenic fracturing process on laboratory-scale Niobrara shale samples," *Journal of Natural Gas Science and Engineering*, vol. 48, pp. 169–177, 2017.
- [30] C. Cai, Y. Yang, J. Liu et al., "Downhole transient flow field and heat transfer characteristics during drilling with liquid nitrogen jet," *Journal of Energy Resources Technology*, vol. 140, no. 12, 2018.
- [31] S. Zhang, Z. Huang, H. Zhang et al., "Experimental study of thermal-crack characteristics on hot dry rock impacted by liquid nitrogen jet," *Geothermics*, vol. 76, pp. 253–260, 2018.
- [32] X. Wu, Z. Huang, H. Song et al., "Variations of physical and mechanical properties of heated granite after rapid cooling with liquid nitrogen," *Rock Mechanics and Rock Engineering*, vol. 52, no. 7, pp. 2123–2139, 2019.
- [33] X. Wu, Z. Huang, Z. Cheng et al., "Effects of cyclic heating and LN2-cooling on the physical and mechanical properties of granite," *Applied Thermal Engineering*, vol. 156, pp. 99–110, 2019.
- [34] B. Xi and Y. Zhao, "Experimental research on mechanical properties of water-cooled granite under high temperatures within 600°C," *Chinese Journal of Rock Mechanics & Engineering*, vol. 29, no. 5, pp. 892–898, 2010.
- [35] Q. Cheng, X. Wang, and A. Ghassemi, "Numerical simulation of reservoir stimulation with reference to the Newberry EGS," *Geothermics*, vol. 77, pp. 327–343, 2019.
- [36] T. T. Cladouhos, S. Petty, M. W. Swyer et al., "Results from Newberry volcano EGS demonstration, 2010–2014," *Geothermics*, vol. 63, no. C, pp. 44–61, 2016.
- [37] C. Park, J. H. Synn, H. S. Shin et al., "Experimental study on the thermal characteristics of rock at low temperatures,"

International Journal of Rock Mechanics and Mining Sciences, vol. 41, no. 3, pp. 81–86, 2004.

- [38] R. D. Dwivedi, R. K. Goel, V. V. R. Prasad et al., “Thermo-mechanical properties of Indian and other granites,” *International Journal of Rock Mechanics & Mining Sciences*, vol. 45, no. 3, pp. 303–315, 2008.
- [39] M. Cha, N. B. Alqahtani, B. Yao et al., “Cryogenic fracturing of wellbores under true triaxial-confining stresses: experimental investigation,” *SPE Journal*, vol. 23, no. 4, p. 271, 2018.